REVIEW

Check for updates

Aggregation-induced emission materials: a platform for diverse energy transformation and applications

Xue Li, [ID] †[ab] Hao Yang,†[ab] Ping Zheng,[ab] Danmin Lin,[ab] Zhijun Zhang,[a] Miaomiao Kang,*[a] Dong Wang [ID] *[a] and Ben Zhong Tang*[ac]

The sustainable development of the modern economy and society is facing severe challenges, one of which is the irreversible consumption of traditional fossil fuels. Despite diverse new energy sources being exploited, it is still difficult to meet the growing multifarious energy requirements for practical applications. In this context, the exploration of high-performance energy transformation materials that allow diverse energy transformations with high efficiency offers a pertinent solution. Profiting from the facile diversification of energy species and expedient modulation of energy transformation, aggregation-induced emission luminogens (AIEgens), which are a particular category of luminescent materials, are emerging as an ideal platform for diverse energy transformations and applications. In light of the rapid progress of AIEgens in this promising field, this review comprehensively summarizes the major advancements of AIEgens from the perspective of energy transformation. The transformation of four categories of energy, namely, solar, chemical, mechanical, and electrical energies, based on AIEgens is covered in this review, and the following representative applications relying on energy transformation are elaborated in each part. The current challenges and future perspectives in this direction are also emphasized.

[a]*Center for AIE Research, Shenzhen Key Laboratory of Polymer Science and Technology, Guangdong Research Center for Interfacial Engineering of Functional Materials, College of Material Science and Engineering, Shenzhen University, Shenzhen 518060, China. E-mail: wangd@szu.edu.cn; mmkfighting@szu.edu.cn*

[b]*Key Laboratory of Optoelectronic Devices and Systems of Ministry of Education and Guangdong Province, College of Optoelectronic Engineering, Shenzhen University, Shenzhen 518060, China*

[c]*Shenzhen Institute of Aggregate Science and Engineering, School of Science and Engineering, The Chinese University of Hong Kong, Shenzhen, Guangdong 518172, China. E-mail: tangbenz@cuhk.edu.cn*

† The first two authors contributed equally.

1 Introduction

Energy resources have long been recognized to play a vital and irreplaceable role in propelling the advancement of human civilization. The progress achieved by human beings in the early stages relied heavily on fossil fuels, the irreversible consumption of which causes environmental pollution, thus posing a serious challenge to the sustainable development of humanity.[1,2] To solve this issue, diverse new and renewable energy resources, such as solar energy, thermal energy, chemical energy, electrical energy, mechanical energy, *etc.*, are being continuously exploited. Even

Xue Li received her PhD from Tsinghua University in 2021. She is currently conducting her postdoctoral research at Shenzhen University, collaborating with Prof. Ben Zhong Tang and Prof. Dong Wang. Her research interests mainly focus on the development of new functional luminescent materials with AIE characteristics and the exploration of their biomedical applications.

Hao Yang received his PhD from Shanghai Jiao Tong University in 2023. He is currently pursuing postdoctoral studies at Shenzhen University in collaboration with Prof. Ben Zhong Tang, Prof. Dong Wang and Ass. Prof. Zhijun Zhang. His research interests mainly focus on the biomedical applications of AIE-based DNA probes and dyes.

so, it is hard to satisfy the ever-growing demands caused by the rapid progression of the modern economy and society. Thus, for continual global development, the multifarious needs for energy must be satisfied while taking full advantage of the available energy resources, as well as promoting energy harvesting and utilization efficiency.

In this regard, photofunctional materials[3,4] that can undergo energy transformation as desired provide an ideal option to cope with the current issues, and the related research area has become one of the frontier hotspots in multidisciplinary research on materials, physics, energy, chemistry, *etc*.[5] For instance, through energy conversion, solar energy can be captured and converted to electric energy, chemical energy, and heat energy; industrial waste heat can be recovered and converted to electricity.[6,7] So far, various energy conversion materials, including but not limited to photothermal materials, thermoelectric materials, photocatalytic materials, magneto-caloric materials, piezoelectric materials, and phase change
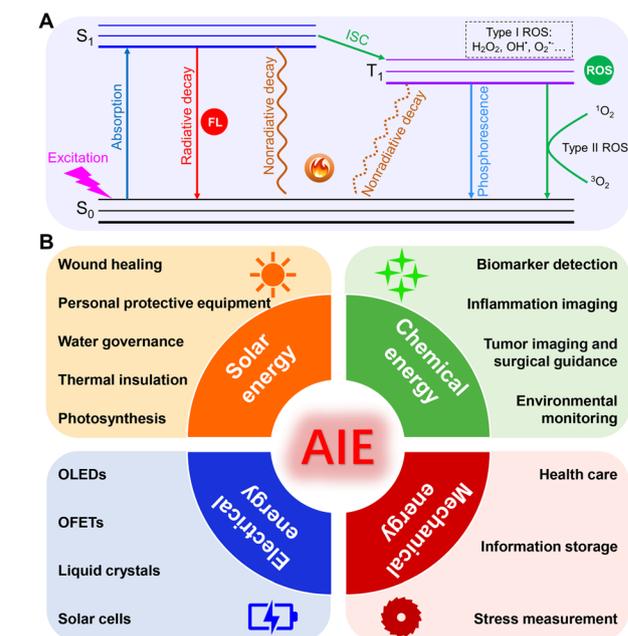

Fig. 1 (A) Jablonski diagram of different decay pathways of luminescent materials. (B) Scheme illustration of various energy conversion and applications based on AIEgens.

materials, have been extensively studied in recent years.[8–11] Beyond that, luminescent materials have also found widespread success in the field of energy transformation and storage,[12,13] because fluorophores could dissipate the absorbed energy *via* diverse channels, such as fluorescence-or phosphorescence-involved radiative decay, heat-associated thermal deactivation as well as reactive oxygen species (ROS)-related intersystem crossing (ISC) (Fig. 1A), thus providing the possibility to convert the simplex energy source to multiple energy species.[14–16]

As a particular type of widely applied luminescent materials, aggregation-induced emission luminogens (AIEgens) have gained substantial attention and have been proven to be an

Miaomiao Kang received her PhD from Sun Yat-sen University in 2018. She studied at the Hong Kong University of Science and Technology as a visiting graduate student under the supervision of Prof. Ben Zhong Tang during 2014–2017. Then, she conducted her postdoctoral research at Shenzhen University, collaborating with Prof. Ben Zhong Tang and Prof. Dong Wang. She is currently an associate researcher at the College of Materials Science and Engineering at Shenzhen University. Her research interests mainly focus on the biomedical applications and exploration of new AIE-active luminescent materials.

Dong Wang received his PhD from Bordeaux University and conducted his postdoctoral study at the University of Toronto and Hong Kong University of Science and Technology. He is currently a distinguished professor at Shenzhen University. His research focuses on the design of AIE luminogens for chemical sensing and biological applications.

Ben Zhong Tang received his PhD from Kyoto University in 1988. He conducted his postdoctoral research at the University of Toronto in 1989–1994. He joined HKUST in 1994 and was promoted to Chair Professor in 2008 and Stephen K. C. Cheong Professor of Science in 2013. He was elected to the Chinese Academy of Sciences in 2009. In 2021, he joined the Chinese University of Hong Kong, Shenzhen. In 2001, he coined the concept of aggregation-induced emission (AIE). His research interests include the exploration of new advanced materials, new luminescent processes and new polymerization reactions.

This journal is © The Royal Society of Chemistry 2023

J. Mater. Chem. A, 2023, **11**, 4850–4875 | **4851**

ideal platform for diverse energy transformations and applications.[17] AIE was initially defined in 2001, and it refers to the unique phenomenon of a category of fluorophores that emit weakly in solution but become exceedingly emissive when clustered into aggregates.[18,19] After 21 years of development, AIE-related studies have pervasively penetrated multiple research domains.[20–23] Particularly, thanks to their abundant intramolecularly rotatable units, twisted molecular configuration, easy tailorability, and modification flexibility, the on-demand energy conversion and exportation have become more convenient because the energy dissipation channels can be readily equilibrated and modulated as desired by tactically adjusting the degree of aggregation as well as the intramolecular motions of AIEgens.[24,25] Specifically, because of the adequate freely-movable rotators or vibrators that ornament the molecular structure, the absorbed energy can be absolutely or largely consumed by the vigorous intramolecular motions of AIEgens in dilute solution, thus yielding relatively weak fluorescence emission but considerable heat generation. Upon aggregation, the nonradiative thermal deactivation was suppressed due to the restriction of intramolecular motions (RIM), accompanied by the amplification of radiative decay, thereby successfully switching on the fluorescence emission.[26] In this context, the ROS-related ISC channel can also be promoted by reducing the singlet–triplet energy gap (ΔE_{s-t}) of AIEgens.[27] More importantly, through relieving the RIM and promoting the intramolecular motions, heat-involved nonradiative decay could also be profitably retained in the aggregate state.[28,29] Taken together, the multi-channel or directional single-channel energy outputs of the excited energy can be successfully achieved as required in the AIE-active energy transformation platform.

Benefitting from these unique advantages of AIEgens in the facile diversification of energy species and the expedient modulation of energy transformation, ground-breaking application advances in this field have been witnessed in recent years. Nevertheless, as far as we know, there is still the need for comprehensive reviews in terms of various AIEgen-facilitated energy transformations. Hence, it is of great significance to systematically summarize the progression of AIEgens from the aspect of various energy transformations. In this review, we intend to provide an overview of the present advancements of AIEgens based on the efficient energy transformation of solar, chemical, mechanical, and electrical energies (Fig. 1B). The underlying transformation principles and design strategies will be briefly described, followed by a particular emphasis on representative applications. Finally, a summary conclusion in association with the discussion of limitations, challenges, and potential opportunities for the future will be provided.

2 Solar energy conversion and applications

Solar energy has been recognized as a type of clean and renewable energy source.[30] As one of the most abundant energy sources with the greatest prospects, the practical utilization of solar energy is rather limited.[31,32] To meet the high demand for energy resources, the highly efficient conversion of solar energy is being extensively pursued. Profiting from the favorable processability, diverse structures, and tunable properties, AIEgens can specifically absorb sunlight across several spectral regions and efficiently convert the solar energy into fluorescence with the desired wavelength, toxic ROS, or heat to cater to the diverse practical application demands by serving as excellent light wavelength transverters, photosensitizers (PSs), and solar-thermal conversion agents. Specifically, through modulating the D–A interaction and π-conjugation degree, the absorption and emission wavelength can be readily tuned. Besides, in pursuit of promoted ROS generation, several strategies such as enhancing the D–A interaction or molecular spin–orbit coupling (SOC), as well as triggering the polymerization or aggregation of AIEgens are generally utilized. On the other hand, efficient photothermal conversion can be obtained by facilitating intramolecular motion. In this respect, molecular rotors or vibrators, and long alkyl chains are generally introduced into the twisted molecular skeleton.[23] In this section, the corresponding applications of the well-designed AIEgens in wound healing, personal protective equipment, water governance, thermal storage, and photosynthesis based on AIEgens-facilitated solar energy transformation will be listed and addressed in detail.

2.1 Wound healing

During the process of wound healing, bacterial infections are a critical factor in hindering wound healing and tissue regeneration.[33,34] Photodynamic therapy (PDT) has been confirmed to be a potential therapeutic approach to fighting against bacterial infections *via* cytotoxic ROS generated by PSs under light irradiation.[35,36] Given that the ΔE_{s-t} of well-tailored AIEgens is small enough, the photo-excited electron would undergo the ISC process to the triplet state, in which energy or electron transfer from the triplet-state AIEgens to surrounding oxygen or substrates occurs, thus generating ROS. Based on the transformation from solar energy to ROS, AIE-active PSs can efficiently eliminate the spread of pathogenic bacteria and contribute to the wound-healing process.

For instance, Tang's group[37] reported that AIEgen-based nanofibers displayed excellent therapeutic efficacy against drug-resistant bacteria and realized the personalized treatment of wound infections (Fig. 2A). The employed AIEgen (TBP) exhibited a broad absorption peaked at 500 nm (Fig. 2B) and typical AIE properties, indicated by the enhanced fluorescence along with the increasing fractions of the poor solvent toluene (Fig. 2C). Besides, upon absorbing light energy, TBP could efficiently generate ROS (Fig. 2D). By using a hand-held electrospinning device, the final AIE nanofibers integrating TBP with poly(ε-caprolactone) were directly obtained on the surface of MASA-infected skin wounds. This *in situ* deposition of AIE nanofibers can minimize bacterial infection and accelerate wound healing upon white light irradiation (Fig. 2E). Aside from AIE-active small molecules, Tang *et al.*[38] also fabricated an AIE active-conjugated polymer (PTB-APFB) with ROS generation

4852 | *J. Mater. Chem. A*, 2023, **11**, 4850–4875

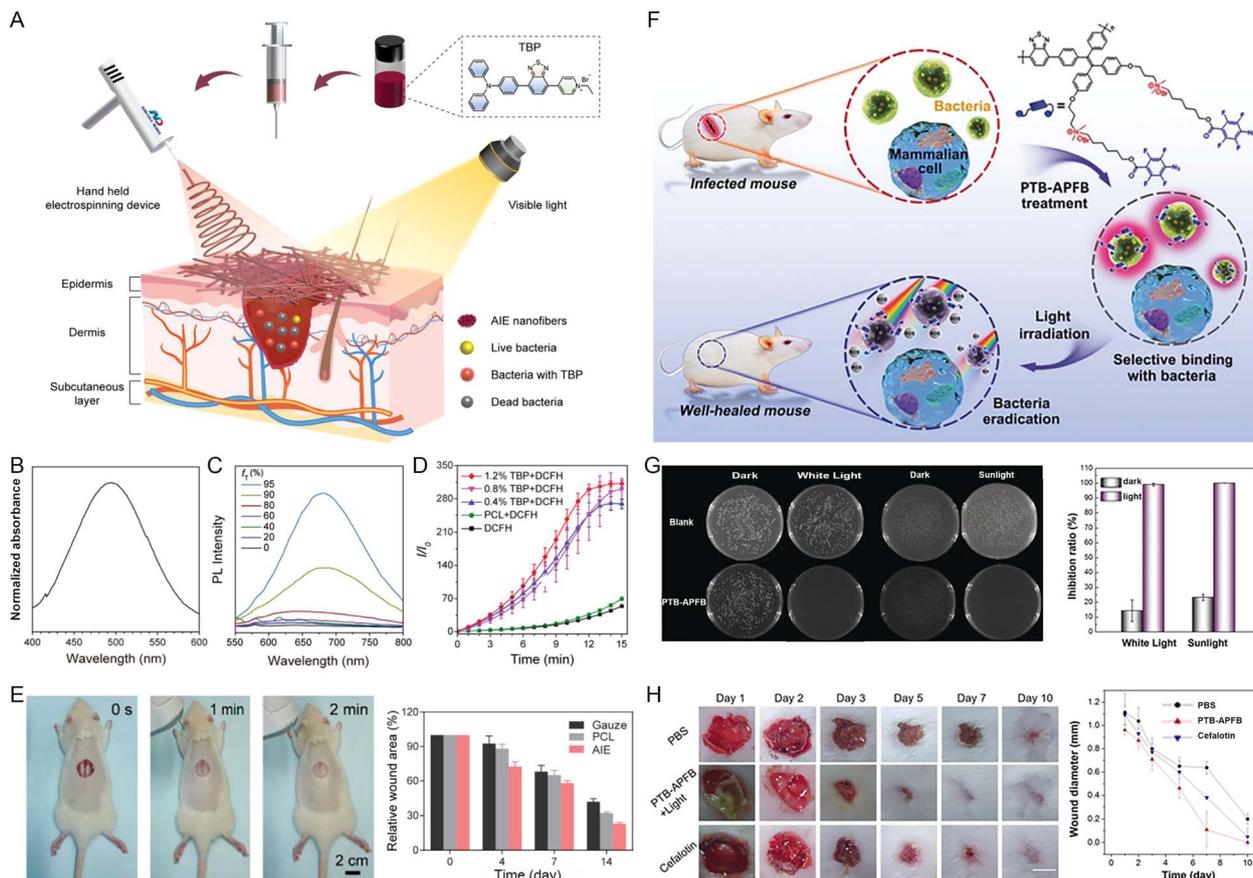This journal is © The Royal Society of Chemistry 2023

Fig. 2 (A) Schematic diagram of the electrospinning–based antibacterial dressing containing AIEgens. (B) The absorption spectrum of TBP in THF solution. (C) PL spectra of TBP in DMSO/toluene mixtures of various toluene fractions (f_T). (D) The ROS generation of PCL nanofibers with 0, 0.4%, 0.8%, and 1.2% of TBP content under irradiation with white light (16 mW cm^{-2}) using DCFH indicator. (E) Photograph of AIE nanofibers deposited in the wounds *in situ* and the proportion of MRSA–infected areas treated with gauze, PCL, and AIE nanofibers containing 1.2% TBP on different days. Reproduced with permission from ref. 37. Copyright 2022, Wiley–VCH. (F) Chemical structure of PTB–APFB and its selective antibacterial application. (G) The biocidal ability of PTB–APFB on *S. aureus* after various treatments. (H) Representative photos of mice wounds infected with *S. aureus* in the periods of different treatments and the quantification of wound healing. Reproduced with permission from ref. 38. Copyright 2020, Wiley–VCH.

capacity to combat bacterial-associated infections (Fig. 2F). The antibacterial activity of PTB-APFB was found to be fantastic *in vitro* and *in vivo* upon mimicking sunlight irradiation as shown in Fig. 2G and H, and was superior to that of the commercial cefalotin.

2.2 Personal protective equipment

In the last few years, with the global outbreak of the coronavirus disease 2019 (COVID-19) pandemic, the demand for personal protective equipment (PPE) sharply increased, and a severe short supply was witnessed for frontline healthcare.[39] What is worse, the commonly used PPEs lack self-cleaning capabilities, and despite being filtered by the PPEs, the viruses or pathogens are not inactivated.[40,41] Once inappropriate discarding of PPEs occurs, the risk of cross-contamination caused by the active viruses or pathogens trapped in the PPEs is significantly increased posing a severe threat to public health.[42,43] To this end, Tang *et al.*[44] empowered PPEs with self-cleaning capability by introducing AIEgens as therapeutic agents. For example,

through a simple method of soaking and solvent evaporation, a range of PPEs such as surgical masks, N95 masks, white gowns, and medical protective suits were incorporated with AIE-active ASCP-TPA (Fig. 3A).[45] Based on the wide absorption scope, and efficient energy conversion from absorbed light to toxic ROS of ASCP-TPA, the rapid and real-time self-antiviral capability of these PPEs against mouse coronavirus murine hepatitis virus A59 (MHV-A59) was achieved even under ultralow-power light irradiation (3.0 mW cm^{-2}) (Fig. 3B and C). Even after washing 100 times or being subjected to 2 weeks of light irradiation, the self-cleaning capability of the obtained PPEs remained almost unchanged, indicating that these PPEs have great potential for reusability and long-term usability. Since biological safety is vitally important for PPEs, the authors systematically evaluated the biocompatibility of ASCP-TPA and ASCP-TPA-attached fabrics (ATaFs) *in vitro* and *in vivo*. The results demonstrated no obvious damage to the normal cells and major organs of the healthy mice, suggesting the excellent biosafety of ASCP-TPA and ATaFs. In addition to AIE PSs, multifunctional AIEgens with concurrent ROS and
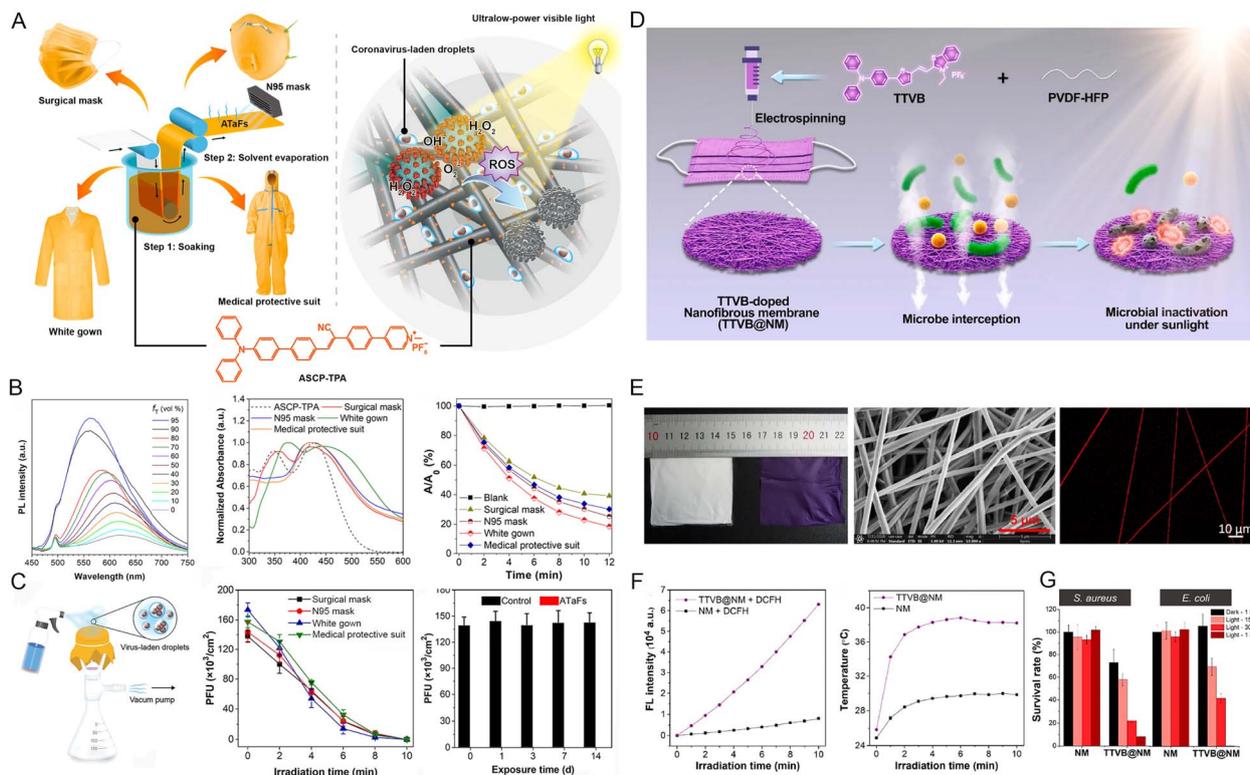
This journal is © The Royal Society of Chemistry 2023

J. Mater. Chem. A, 2023, **11**, 4850–4875 | **4853**

Fig. 3 (A) The chemical structure of ASCP-TPA, the synthesis procedure of ATaFs and various ATaFs-based PPEs, as well as the principle of action of ATaFs against coronavirus under irradiation with ultralow-power light. (B) The PL spectra of ACSP-TPA in DMSO and DMSO/toluene mixtures, the absorption spectra of ASCP-TPA and various PPEs, and the ROS generation of ASCP-TPA and various PPEs under white light irradiation (10 mW cm^{-2}). (C) The setup for simulating the process wherein PPEs capture viral aerosols, the virucidal efficiency of various PPEs after different irradiation times (3 mW cm^{-2}), and the retained virucidal function of ATaFs after continuous exposure to office light for different numbers of days. Reproduced with permission from ref. 45. Copyright 2021, American Chemical Society. (D) Schematic of the TTVB-loaded nanofibrous membrane (TTVB@NM) prepared by electrospinning for bioprotective function. (E) Photographs of NM and TTVB@NM, SEM and CLSM image of TTVB@NM. (F) Total ROS production and the photothermal conversion efficiency of TTVB@NM. (G) The survival percentages of microbes treated with NM and TTVB@NM under simulated sunlight irradiation. Reproduced with permission from ref. 46. Copyright 2021, Elsevier.

photothermal conversion abilities were employed. Another work reported by Tang and coworkers[46] demonstrated that the TTVB-doped nanofibrous membrane (TTVB@NM) represented a promising candidate for bioprotection. The broad absorption in the visible range, eminent ROS generation capacity, and mild photothermal conversion performance of TTVB endowed TTVB@NM with sunlight-triggered photodynamic/photothermal anti-pathogen functions (Fig. 3D). After being coated on the surface of the mask, the multi-layered porous structure of TTVB@NM can effectively intercept pathogenic droplets and aerosols (Fig. 3E). The excellent energy transformation of TTVB led to 99% inactivation for bacteria, 88% inhibition for fungi, and 99% inhibition for bacteriophages under simulated sunlight irradiation for only 10 min (Fig. 3F and G). The good survival rate of bacteria, fungi, and bacteriophage incubated with TTVB in dark conditions implied the good biosafety of TTVB without light irradiation.

2.3 Water governance

The importance of freshwater for life is evident.[47,48] Despite the abundance of water resources on the earth, the vast majority is

seawater (accounting for 97.5% of total water resources), which cannot be used directly. Moreover, the water scarcity crisis is further aggravated by the inevitable environmental deterioration and water pollution along with the rapid development of the global economy.[49,50] Under these circumstances, obtaining freshwater from the seemingly inexhaustible seawater by solar-driven water evaporation indicates a promising direction for addressing the global water resource challenges.[51–53] High-efficiency water evaporation requires efficient solar-thermal conversion materials to transform solar energy into heat. For example, a croconium derivative (named CR-TPE-T) reported by Gu *et al.*[54] represented a promising organic small solar-thermal conversion agent. It was demonstrated that CR-TPE-T with unique biradical and powerful π–π stacked solid properties exhibited a broad absorption spectrum from 300 to 1600 nm to effectively harvest sunlight. Meanwhile, the photothermal efficiency as high as 72.7% under 808 nm laser irradiation was also assessed. Based on this, the solar-steam-generation performance of CR-TPE-T was up to 87.2%, and the water evaporation rate of 1.272 kg m^{-2} h^{-1} was captured under 1 sun irradiation.

Another example was reported by Tang and coworkers,[55] who designed an AIEgens-loaded three-dimensional all-fiber aerogel

4854 | *J. Mater. Chem. A*, 2023, **11**, 4850–4875

This journal is © The Royal Society of Chemistry 2023

(3D AFA) for interface solar steam generation. Due to its highly interconnected porous structure and light weight as shown in Fig. 4A, the 3D AFA can float on the water surface and continuously pump water. The employed AIEgens (MTTT-BT) displayed a relatively broad absorption spectrum and favorable photothermal conversion performance (Fig. 4B). With the assistance of 3D AFA, a superior solar absorbance with wide absorption scope covering a wavelength range of 200–2500 nm and a higher temperature increment were detected (Fig. 4C). These properties endowed the obtained 3D AFA with a high evaporation rate (1.43 kg m^{-2} h^{-1}) and solar-to-vapor conversion efficiency (86.5%) under the irradiation of 1 sun. Even under natural light irradiation, the evaporation rate could also arrive at 10.9 kg m^{-2} h^{-1} (Fig. 4E). These examples suggest that AIEgens could perform well in the field of water evaporation by serving as an efficient solar-thermal conversion agent.

In the process of solar-driven interfacial steam generation, a warm and moist atmosphere usually forms around the evaporator, which will provide a suitable environment for the growth of microorganisms. The presence of microorganisms would seriously impair the service life of the evaporator, in particular in wastewater treatment.[56] Based on these considerations, Wang and coworkers[57] employed AIEgens with solar-thermal and solar-ROS conversion capabilities as solar absorbers to achieve efficient solar steam evaporation and biofouling

prevention. They firstly doped AIE-active TPA-BTDH judiciously engineered with a typical D–A–D structure and large twisted angles into a 3D nanofiber by electrospinning (Fig. 5A). TPA-BTDH demonstrated a broad absorption spectrum, near-infrared (NIR)-I fluorescence emission spectrum, as well as efficient ROS and heat generating abilities (Fig. 5B). In the handcrafted evaporation system displayed in Fig. 5C, the steam of the simulated seawater containing five significant ions (Na$^+$, Mg^{2+}, K$^+$, Ca^{2+}, and Pb^{2+}) was generated under 1 sun illumination and then condensed on the inner wall of the glass. After this purification process, the concentration of ions in the evaporated water was reduced from 10^3 to 10^{-1} mg L^{-1}. Additionally, the wastewater containing four types of bacteria (*E. coli*, *S. epidermidis*, *S. aureus*, MRSA) could also be depurated using this evaporation system. No bacterial cloning was observed in the condensate after water evaporation, indicating the effectiveness of this system in bacteria removal (Fig. 5D). These results powerfully demonstrated that this AIEgen-doped evaporator could efficiently purify seawater and wastewater *via* fully utilizing solar energy.

Another challenge that exists in the field of water governance is the harmful algae blooms (HABs), which potentially impair ecosystems, human health, and economic development.[58–60] To address this issue, Luo *et al.*[61] developed a novel positively charged AIEgen TVP-A. The inherent positive charge endowed
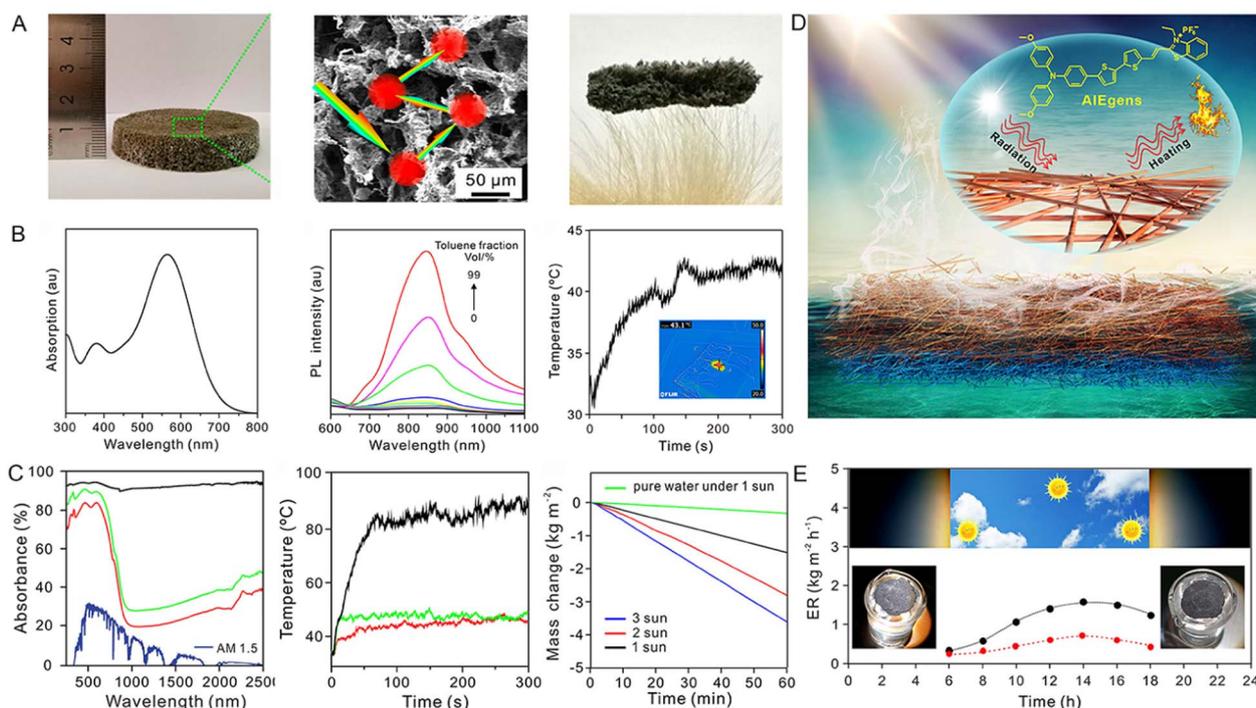

Fig. 4 (A) Bright photograph, SEM image, and ultralow density of 3D AFA. (B) The absorption and PL spectra of MTTT-BT in DMSO and DMSO/toluene mixtures with various toluene fractions, and the photothermal performance of the MTTT-BT in the solid state under 1 sun irradiation for 300 s. (C) The absorption spectrum of the 3D AFA across 250−2500 nm and solar spectral irradiance measured by standard AM 1.5 G solar radiation, temperature shift of the 3D AFA and nanofiber mat with different contents of MTT-BT under 1 sun irradiation (1 kW m^{-2}), and water loss of 3D AFA with time at different light intensities. (D) Schematic illustration of solar steam generation. (E) Water evaporation rate of 3D AFA (black spots) from 6 : 00 to 18 : 00 for a day (red spots indicated the evaporation rate of a blank beaker with no 3D AFA) under natural sunlight. Reproduced with permission from ref. 55. Copyright 2020, American Chemical Society.
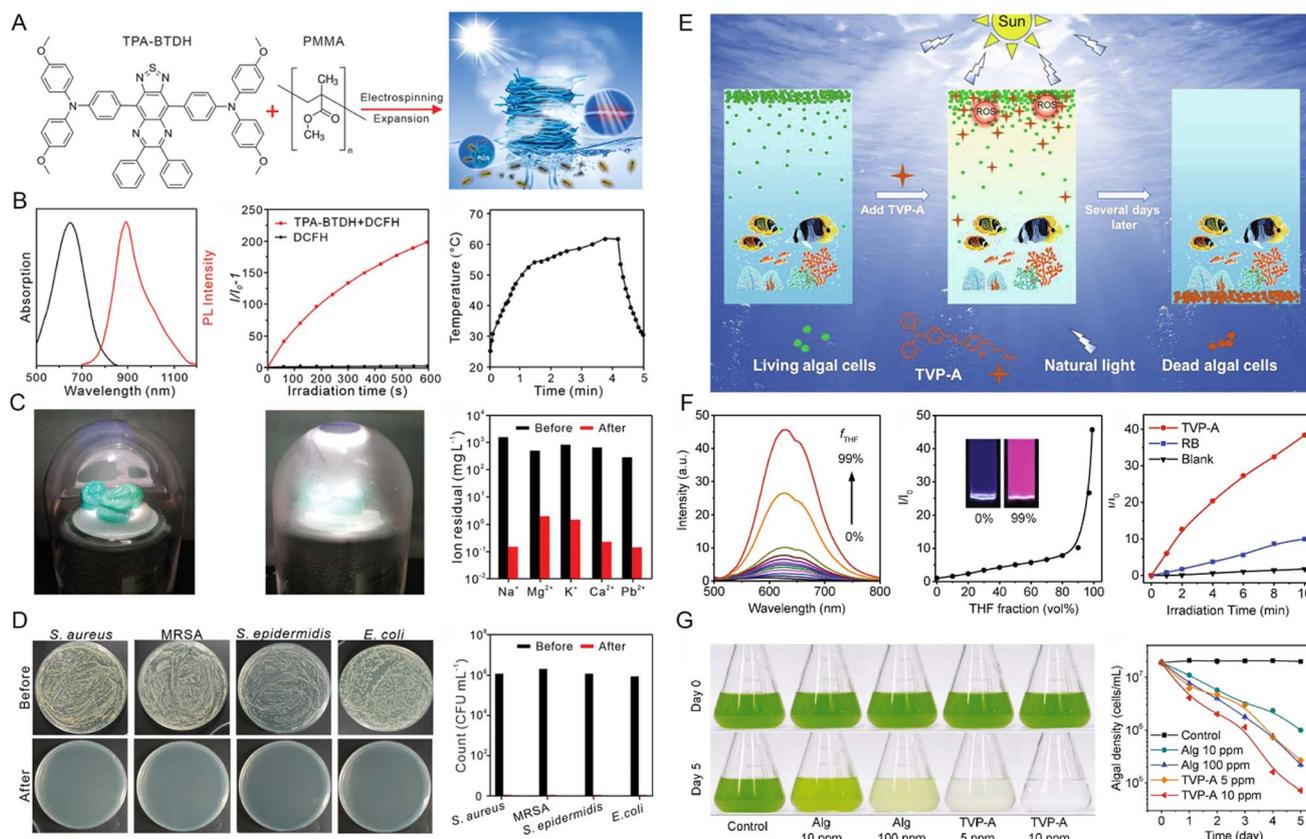
This journal is © The Royal Society of Chemistry 2023

J. Mater. Chem. A, 2023, **11**, 4850–4875 | **4855**

Fig. 5 (A) The chemical structure of TPA-BTDH and schematic illustration of the experimental concept for the side area-assisted evaporator. (B) The absorption and PL spectra of TPA-BTDH in THF solution, ROS production of TPA-BTDH under xenon lamp irradiation determined by DCFH, and the photothermal conversion of TPA-BTDH in powder upon 1 sun irradiation. (C) Photograph of a handmade solar steam generating device, including a glass cover, an AFPCF evaporator, and a dewar filled with seawater or wastewater and clean water cemented on the inner wall of the glass cover and the contents of several ions in the evaporated simulated seawater and clean water. (D) Photographs of the microbe (*S. aureus*, MRSA, *S. epidermidis*, and *E. coli*)-inoculated agar plates; the microbes were from simulated wastewater or the collected water after evaporation. Reproduced with permission from ref. 57. Copyright 2021, Wiley-VCH. (E) Schematic diagram of the removal of algal blooms selectively by TVP-A with natural light irradiation. (F) Fluorescence spectra of TVP-A and the relative FL intensity of TVP-A at 625 nm in H$_2$O/THF mixtures with different fractions of THF, and ROS generation of TVP-A (5 μM) under white light irradiation for 10 min, determined by DCF-DA. (G) Photographs of *C. reinhardtii* (1.6×10^7 cells mL^{-1}) on Day 0 and day 5 treated with Alg (10 ppm and 100 ppm) or TVP-A (5 ppm and 10 ppm) and its efficacy in the clearance of blooms caused by *C. reinhardtii* under simulated daily cycling. Reproduced with permission from ref. 61. Copyright 2020, Elsevier.

TVP-A with good aqueous solubility and allowed its attachment to algal cells floating on the water's surface. Under light irradiation, the AIE-active TVP-A could generate ROS efficiently, thus provoking algal cell death (Fig. 5E and F). The comparison experiment in algal bloom control demonstrated that only 5 ppm of TVP-A was effective in removing the algal bloom after 5 simulated natural daily cycles. In contrast, inadequate clearance of algal cells was observed even when the concentration of a commercial algaecide (Alg) increased to 100 ppm, clearly suggesting the superior applicability of TVP-A for HABs removal (Fig. 5G).

2.4 Thermal storage

Maintaining normal body temperature is essential for the somatic cells to perform normal physiological functions. Photothermal nanofibers, which can convert solar light into thermal energy, are an ideal option for the preparation of smart textiles.[62] To meet the practical application demands of photothermal nanofibers, functional agents with high photothermal conversion efficiency are needed. Using reverse thinking of the AIE principle, Wang *et al.*[63] constructed a core–shell nanofiber by coaxial electrospinning technology, in which the olive oil solution of AIEgens (BPBBT) serves as the core and PVDF-HFP constitutes the shell. This core–shell structure ensured the molecularly dissolved state of AIEgens in olive oil as well as the resulting sufficient intermolecular movements within the fiber, thus amplifying the nonradiative energy dissipation and boosting the photothermal conversion efficiency of fibers (Fig. 6A). The thermal generation and preservation ability of the obtained nanofiber was validated. As illustrated in Fig. 6B, a rapid temperature rise in the core–shell fiber sheet from about 20 to 51.2 °C was detected after covering the volunteer's knee. Moreover, the temperature could still increase to around 24 °C under natural sunlight
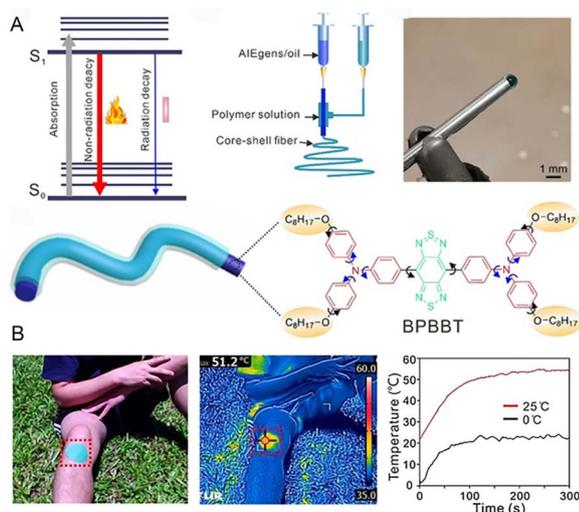
4856 | *J. Mater. Chem. A*, 2023, **11**, 4850–4875

This journal is © The Royal Society of Chemistry 2023

Fig. 6 (A) Jablonski diagram, setup of coaxial electrospinning, photograph of the core–shell needle, the structure of a core–shell fiber, and the molecular structure of BPBBT. (B) The optical and infrared images of a photothermal patch to warm the volunteer's knee in natural sunlight, and the temperature shift of BPBBT CS-3 at different ambient temperatures of 0 and 25 °C. Reproduced with permission from ref. 63. Copyright 2020, Wiley-VCH.

irradiation even if the initial temperature was set to 0 °C. This work represents a wonderful protocol to boost the photothermal efficiency of fibers and indicated the promising application potentials of AIEgens in the field of heating textiles.

In the field of solar-thermal conversion and storage, visually monitoring the solar-thermal energy storage process is significantly beneficial for the improvement of energy utilization.[64,65] Given these circumstances, Liu *et al.*[66] developed fluorescent thermochromic wood-based composite phase change materials (WPCMs) to visualize solar-thermal energy conversion and storage. In their work, carbon dots with AIE characteristic (AIE-CDs) were employed as photothermal conversion and fluorescent display materials thanks to their excellent sunlight absorbance and transformation capacities, as well as distinct optical properties in the dissolved and aggregate states. AIE-CDs, exhibiting individual blue and red emissions in the dispersed and aggregate state, respectively, together with polyethylene glycol (PEG), were encapsulated in the delignified wood (DW). Without solar irradiation, AIE-CDs emitted red fluorescence, gradually decreasing and switching to blue emission upon solar radiation. This is because the solar-thermal conversion-resulted in the solid–liquid transformation of WPCMs which facilitated the dissolution of AIE-CDs, thereby regulating the emission color. This work represents the first simultaneous exploitation of AIE-CDs in solar-thermal conversion, storage, and monitoring.

2.5 Photosynthesis

Photosynthesis refers to the process of transforming carbon dioxide and water into carbohydrates inside the chloroplasts with the assistance of solar energy. This natural process provides the requisite energy and oxygen for nearly all living things on the earth.[67,68] Given the high dependence on solar energy, improving the light-harvesting ability will be conducive to photosynthesis.[69] Despite the wide spectral range of the sunlight radiated to the earth, including ultraviolet (UV) (300–400 nm), visible (400–700 nm), and infrared regions (700–2500 nm), the chloroplasts can only utilize light energy in the visible wavelength range (400–700 nm), which is known as photosynthetically active radiation (PAR) (Fig. 7A).[70] In this context, thanks to their unique merit of large Stokes shifts, AIEgens can red-shift the undesirable UV light to the favorable visible region. Particularly, more precise wavelength conversion could also be achieved within the visible region, thus resulting in significantly increased light utilization and enhanced photosynthesis rate.

For example, to enhance the biofuel and lipid productivity of microalgae, Kim *et al.*[71] employed an AIEgen-based photoconverting fluorescent film to convert green light (400–600 nm) to red light (600–700 nm) because the 600–700 nm light was demonstrated to be more effective than 500–600 nm light in promoting microalgal growth. Owing to the unparalleled solid-state optical properties and good biocompatibility, a 28.8% increase in the total fatty acid methyl ester was achieved by the AIEgen-based light-converting film. They also demonstrated that the deep red region (650–700 nm) was more beneficial than the 600–650 nm region in boosting the photosynthesis rate of *Chlorella* sp. (Fig. 7B). In addition to *Chlorella* sp., the growth of *Cyanobacteria* can also be promoted by employing AIEgens as light wavelength converters.
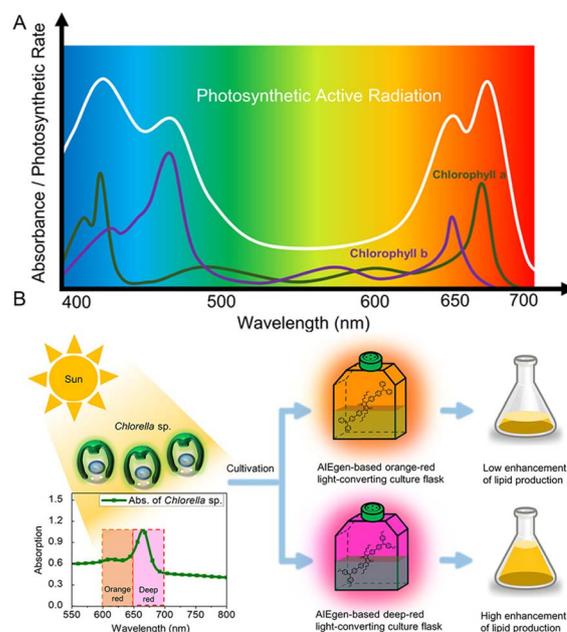

Fig. 7 (A) The absorption spectra of chlorophyll and photosynthetically active radiation (PAR). (B) Schematic illustration showing that *Chlorella* sp. can utilize the solar energy more efficiently in the AIEgen-based deep-red light-converting culture flask. Reproduced with permission from ref. 71. Copyright 2020, American Chemical Society.

3 Chemical energy conversion and applications

Chemical energy refers to the energy absorbed or released during chemical reactions. To utilize this kind of energy, chemiluminescence resonance energy transfer (CRET) was first proposed in 1967.[72] A CRET system usually consists of chemiluminescence (CL) donors (*e.g.*, peroxyoxalate,[73,74] lucigenin,[75–77] luminol,[78–80] $KMnO_4$,[81] *etc.*) and suitable acceptors (*e.g.*, fluorescent dyes,[82,83]) in which the chemical energy released by the CL reaction can further chemically excite adjacent fluorophores *via* nonradiative energy transfer to emit fluorescence.[84,85] Without the need for an external excitation source, the CRET system can effectively avoid the limitation of excitation light sources, eliminate the photoexcitation-caused photobleaching and autofluorescence, as well as exhibit low background and high sensitivity.[86–89] Bearing excellent optical properties (*e.g.*, tunable absorption and emission wavelength range, large Stoke's shift, high fluorescence quantum efficiency in aggregates), AIEgens represent ideal candidates for serving as fluorescent acceptors in the CRET systems, thus enabling the efficient transformation of chemical energy to fluorescence emission. Regarding the construction of AIEgens-involved CRET systems, AIEgens with twisted molecular geometry are preferred as the intermolecular π–π stacking interactions-caused nonradiative thermal deactivation can be largely suppressed.[90] Particularly, the distance between the energy donor and the AIE-active energy acceptor should be finely controlled to ensure CRET efficiency.[91] By employing well-defined AIEgens in the CRET systems, the chemical energy can be effectively converted to luminescence and various applications involving the detection of biomarkers, inflammation imaging, tumor imaging, imaging-guided therapy, as well as environmental monitoring have been witnessed. In this section, some representative examples will be addressed in detail to elaborate on the progression of AIEgens-based chemical energy conversion.

3.1 Detection of biomarkers

Biomarkers are used as measurable, quantifiable indicators of pathological or biological processes to predict the onset and progression of a disease.[92] With the development of chemiluminescence synthesis technology, chemiluminescence has been widely used in medical laboratory science.[93] Owing to the high energy transfer from the excited-state chemical substrate to the AIEgens, the enhancement of fluorescence can offer benefits for the detection of certain biomarkers.

As the primary ROS, the superoxide anion ($O_2^{\bullet-}$) plays an essential role in biological and physiological processes. It is very important to monitor the $O_2^{\bullet-}$ as it is either protective or deleterious in the clinical context.[94] Tang *et al.*[95] designed a novel sensing platform (TPE-CLA) with turn-on property by conjugating the imidazopyrazinone (CLA) unit for $O_2^{\bullet-}$ detection with the TPE skeleton for AIE activation (Fig. 8A). Due to the hydrophilicity, TPE-CLA was non-emissive in aqueous solution, enabling the turn-on detection for $O_2^{\bullet-}$. Specifically, benefitting from the large overlap between the CL emission of
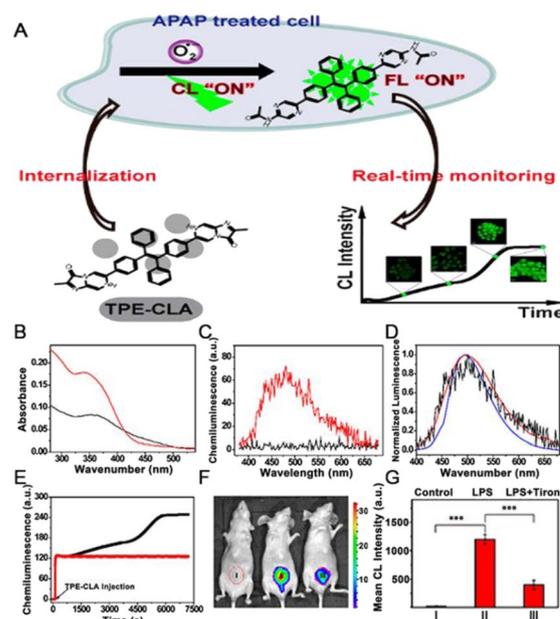

Fig. 8 (A) Chemical structure of TPE-CLA, and schematic illustration of the dual FL/CL sensing of endogenous $O_2^{\bullet-}$ in live cells. (B) Absorption spectra of 20 μM TPE-CLA (1.0% CH_3OH) before (black) and after (red) reaction with 50 μM $O_2^{\bullet-}$. (C) CL spectra of 10 μM TPE-CLA (0.5% CH_3OH) before (black) and after (red) reaction with 30 μM $O_2^{\bullet-}$. (D) Normalized FL spectra (blue, λ_{ex} = 350 nm), CL (black) spectra of 10 μM TPE-CLA (0.5% CH_3OH) reacted with 30 μM $O_2^{\bullet-}$, and FL spectra (red, λ_{ex} = 350 nm) of TPE-PZA (10 μM, 0.5% THF). (E) Real-time CL monitoring of $O_2^{\bullet-}$ in HL-7702 cells stimulated by PBS (red line) and overdosed APAP (20 mg mL^{-1}) (black line) with TPE-CLA (200 μM) injection. (F) CL imaging of $O_2^{\bullet-}$ in LPS-treated mice; (I) Saline + TPE-CLA (200 μM, 200 μL), (II) LPS (1 mg mL^{-1}, 200 μL) + TPE-CLA (200 μM, 200 μL), (III) LPS (1 mg mL^{-1}, 200 μL) + Tiron (20 mM, 200 μL) + TPE-CLA (200 μM, 200 μL). (G) Quantification of CL intensity in different groups. Reproduced with permission from ref. 95. Copyright 2017, American Chemical Society.

CLA and the absorption of the final product TPE-PZA (Fig. 8B), efficient CRET was able to occur from the CLA moiety to TPE-PZA. As shown in Fig. 8C, TPE-CLA exhibited distinctly enhanced CL once reacted with $O_2^{\bullet-}$. The high consistency of the fluorescence (FL)/CL spectrum of TPE-CLA after reaction with $O_2^{\bullet-}$ and the FL spectrum of TPE-PZA verified that the AIE-active TPE-PZA was responsible for the turn-on response of both FL and CL. Finally, the ability of TPE-CLA to monitor $O_2^{\bullet-}$ *in vitro* and *in vivo* was confirmed, respectively (Fig. 8E–G). The reaction-activated AIE effect and dual FL/CL detection were successfully achieved in this study, which represented a typical example involving chemical energy transformation and biomarker detection.

The precise and sensitive detection of biomarkers is essential for diagnosing disease, but developing simple sensing probes remains challenging.[96] Creatinine (CRN) is a preferred marker for renal insufficiency, and it is essential to develop inexpensive, robust, and accurate methods to monitor CRN in body fluids.[97] Khataee *et al.*[98] developed a highly sensitive CRN probe using water-soluble CuNCs with AIE behavior. In the presence of Al^{3+} ions, CuNCs formed aggregates through GSH-

4858 | *J. Mater. Chem. A*, 2023, **11**, 4850–4875

This journal is © The Royal Society of Chemistry 2023

Al^{3+} interactions, resulting in substantial fluorescence enhancement. In contrast, the coordination of CRN and Al^{3+} ions led to the depolymerization of CuNCs aggregates. In addition, Liang et al.[99] designed an electrochemiluminescence (ECL) doping-free film based on AIEgen to achieve the sensitive detection of dopamine (DA) with a wide linear range (0.05–350 μM) and a detection limit of 17.0 nM. To overcome the narrow detection range and poor quantitative reproducibility of commercial CL indicators for western blot, Zhu et al.[100] developed an AIE-based enzyme-activated fluorescent indicator (DQM-ALP) by introducing alkaline phosphate (ALP)-triggered hydrophilic phosphate group into an AIE building block of quinolline-malononitrile (QM). The obtained DQM-ALP can be dispersed well in both water and lipid environments to show initial "off" fluorescence. When exposed to ALP-coupled secondary antibodies on PVDF membranes, DQM-ALP could be cleaved to release the hydrophobic QM-OH to emit intense luminescence, thus achieving the "off–on" detection of proteins. Owing to the excellent signal stability as well as the high concentration-induced fluorescence enhancement of the AIE core, DQM-ALP was able to improve the quantitative reproducibility, and also expand the linear quantification range fluorescence western blot assay.

Covalent organic frameworks (COFs) as an emerging class of crystalline porous nanomaterials with periodic structure and extensive surface areas[101] have also been employed. For instance, Li et al. prepared a fluorescent COFs material TPE@SNW-1 with strong AIE properties by integrating a weak fluorescent Schiff base network (SNW-1) with TPE. Then, a CRET platform was constructed with TPE@SNW-1 serving as the energy acceptor and bis(2,4,6-trichlorophenyl) oxalate (TCPO)-hydrogen peroxide H_2O_2 reaction acting as the energy donor. Based on this CRET system, the uric acid content in human serum can be successfully determined indirectly in the presence of uricase.[102]

3.2 Inflammation imaging

As is well known, inflammation is a physiological response to injurious stimuli caused by infections, pathogens, or immune responses, and a series of problems arise once the inflammation gets out of control.[103,104] Nevertheless, available methods for monitoring inflammation are limited; for example, the inflammatory process cannot be monitored in real-time, nor can the dynamic course of the pathological process be provided.[105] Under these circumstances, CL imaging is perhaps a favourable approach for keeping track of inflammation.

For example, Lv et al. reported a distinct CL nanosensor (termed NTPE-PH), which was formed from AIEgen (TPE-PH).[106] When a CL moiety in NTPE-PH was burnt, the NTPE-PH could be excited by the released reaction energy, subsequently producing CL. Owing to the ultrahigh concentrated CL moieties in one nanoparticle, NTPE-PH exhibited extremely high sensitivity to $^1O_2$ and largely amplified CL in the region of acute and chronic inflammations. In the accompanying study, mouse models of arthritis and peritonitis could be diagnosed through in vivo NIR imaging by using a delicately tailored nanoparticle

imaging probe (CLNP-PPV/BDP), which consisted of an inflammatory H_2O_2-responsive peroxalate (CPPO) as a chemical fuel, a low-bandgap AIE-conjugated polymer (DPA–CN–PPV) as a bright NIR emitter, and an energy gap-bridging photonic molecule (BODIPY).[107] Furthermore, a highly emissive NIR-II AIEgen, named TPE-BBT, was reported by Tang and colleagues.[108] TPE-BBT possessed the highest quantum yield (QY) value among organic molecules, showing an absolute QY of up to 10.4%. They further prepared the TPE-BBT chemiluminescent nanoparticles (CLNPs), which consisted of CPPO serving as the chemiexcitation agent, a NIR-I emissive fluorescent dye (BTD540) working as the energy bridge, and TPE-BBT acting as the NIR-II emissive energy acceptor. Bright NIR-II emission was observed after a series of processes, including the reaction between CPPO and H_2O_2, the generation of the high-energy 1,2-dioxetanedione (DOD) intermediate, chemiexcitation of BTD540, and Förster resonance energy transfer (FRET) between BTD540 and TPE-BBT. Owing to the efficient CRET and FRET, TPE-BBT displayed excellent CL imaging quality in the local arthrosis inflammation in mice with a high signal-to-background ratio (SBR) of 130. These studies demonstrated the excellent clinical potential of AIEgens as chemical energy transverters to emit fluorescence.

Beyond CL imaging, afterglow luminescence imaging has been the focus of intensive research during the past few years. Recently, Ding et al.[90] reported a dual-responsive afterglow fluorescent nanoprobe for understanding neutrophil-involved inflammatory diseases. The nanoprobe was prepared by employing an amphiphilic lipid-PEG copolymer to encapsulate both the enol ether precursor of Schaap's 1,2-dioxetane with phenylborate moiety (AGL) and a highly NIR emissive AIEgen (TPE-TV-CyP) (Fig. 9A and B). The tactical design with a 3D twisted molecular structure was beneficial for augmenting the intensity and duration of NIR afterglow luminescence by reducing nonradiative heat inactivation. This tactically designed nanoprobe exhibited dual responsiveness to both environmental pH and $ONOO^-$ (Fig. 9C and D). It can be seen from the in vivo imaging results that the activated afterglow signal at the acute inflammatory site reached a maximum at 2 h with an ultrahigh SBR of 461.3, suggesting that the generation level of $ONOO^-$ peaked at 2 h (Fig. 9E). These results were in accordance with the immunofluorescence staining data of neutrophils in Fig. 9F. The designed nanoprobe can also be utilized to successfully distinguish inflammation from allergy, considering the peculiar infiltration of neutrophils at the site of inflammation (Fig. 9G). These results strongly support that AIEgens could emit fluorescence or afterglow luminescence via efficient chemically generated energy transfer.

3.3 Tumor imaging and surgical guidance

Globally, cancer is undeniably one of the most refractory and deadly diseases that seriously threaten human health. Due to the high mortality and increased morbidity of cancer, early detection was deemed to be a prerequisite for fighting against cancer.[109] At present, ultrasound, computed tomography (CT), and magnetic resonance imaging (MRI) serve as conventional

This journal is © The Royal Society of Chemistry 2023

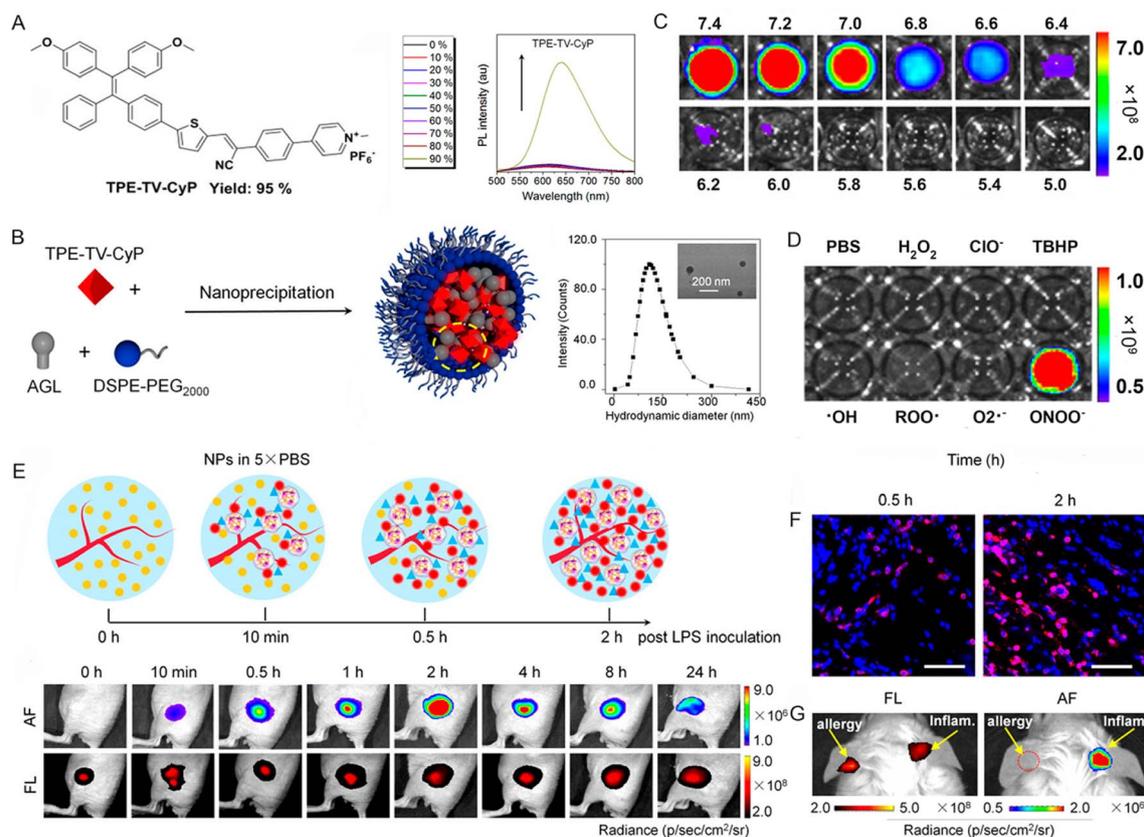J. Mater. Chem. A, 2023, **11**, 4850–4875 | **4859**

Fig. 9 (A) The chemical structure of TPE-TV-CyP and PL spectra of TPE-TV-CyP in the THF/water mixtures with different water fractions. (B) Schematic illustration showing the preparation of the NPs, size distribution, and TEM image (inset) of the PA-AGL NPs. (C) Afterglow luminescence activation of the pre-irradiated PA-AGL NPs after 200 μM ONOO$^-$ was added to PBS solutions with different pH values. (D) Specificity of the pre-irradiated PA-AGL NPs to ONOO$^-$ in PBS at pH 7.4. (E) Illustration of dynamic changes in neutrophil infiltration, ONOO$^-$ production, and representative time-dependent images of afterglow and NIR fluorescence of the acute inflammatory lesions by the *in situ* administration of pre-irradiated PA-AGL NPs in 5 × PBS (pH 7.4) after LPS inoculation. (F) Immunofluorescence staining of neutrophils at the sites of acute inflammation (red: Gr-1; blue: DAPI). Scale bars, 50 μm. (G) NIR fluorescence and afterglow images of the allergic (left) and LPS-induced inflammatory (right) mouse ear injected with the pre-irradiated PA-AGL NPs in Milli-Q water after 0.5 h of LPS inoculation. Reproduced with permission from ref. 90. Copyright 2022, American Chemical Society.

screening methods for tumors.[110] However, these techniques have some limitations, such as low sensitivity, radiative threat, low accuracy, poor adherence, *etc*.[111] Benefitting from the extremely high sensitivity, no external excitation source, and excellent SBR, chemiluminescence has been spotlighted as a compassionate, non-invasive approach in recent years and it has been utilized in the early diagnosis of tumors, and real-time navigation during surgical operations.

For instance, Tang and coworkers[112] reported a chemically conjugated NIR CL emitter with AIE features, named TBL. The chemiluminescence emitted by the obtained TBL dots can continue for over 60 min. Owing to the NIR emission, the CL can penetrate through tissues impressively with a total thickness of more than 3 cm. Also, TBL dots perform well in distinguishing tumors from normal tissue through CL imaging. Furthermore, to obtain a trigger-controlled, bright, and enriched CL signal, a dual-lock strategy using two sequential triggers of analyte and light was reported by Zhu *et al*.[113] Specifically, the masking group of the AIE-active probe (QM-B-CF) can be removed by the analyte (*e.g.*, H$_2$O$_2$), leading to the

accumulation of the pre-chemiluminophores (QM-O$^-$-CF). The electron-rich double bond can be further activated by light and trigger the *in situ* generation of 1,2-dioxetane *via* a free-radical addition reaction, thus exhibiting an enriched and bright CL signal (Fig. 10A). Due to the AIE property of QM-O$^-$-CF (Fig. 10B), AIE fluorescence was also observed in addition to the amplified CL signal. The significantly enhanced CL signal of QM-B-CF in the presence of H$_2$O$_2$ upon light irradiation solidly suggested the feasibility of this strategy (Fig. 10C). The *in vivo* tumor imaging was further conducted in the 4T1 tumor-bearing mouse model, which exhibited overexpressed H$_2$O$_2$ in the tumor site. As shown in Fig. 10D, dual-model tumor imaging involving FL imaging and CL imaging was achieved upon the intra-tumoral injection of QM-B-CF. Particularly, light irradiation was needed for CL imaging. After the addition of the antioxidant agent NAC (*N*-acetylcysteine, an H$_2$O$_2$ scavenger), both the FL and CL signal largely decreased, indicating the unsuccessful forming of QM-O$^-$-CF (Fig. 10D). The constructed sequentially responsive CL probes do not merely improve the resolution of CL imaging, but also provide a new avenue for
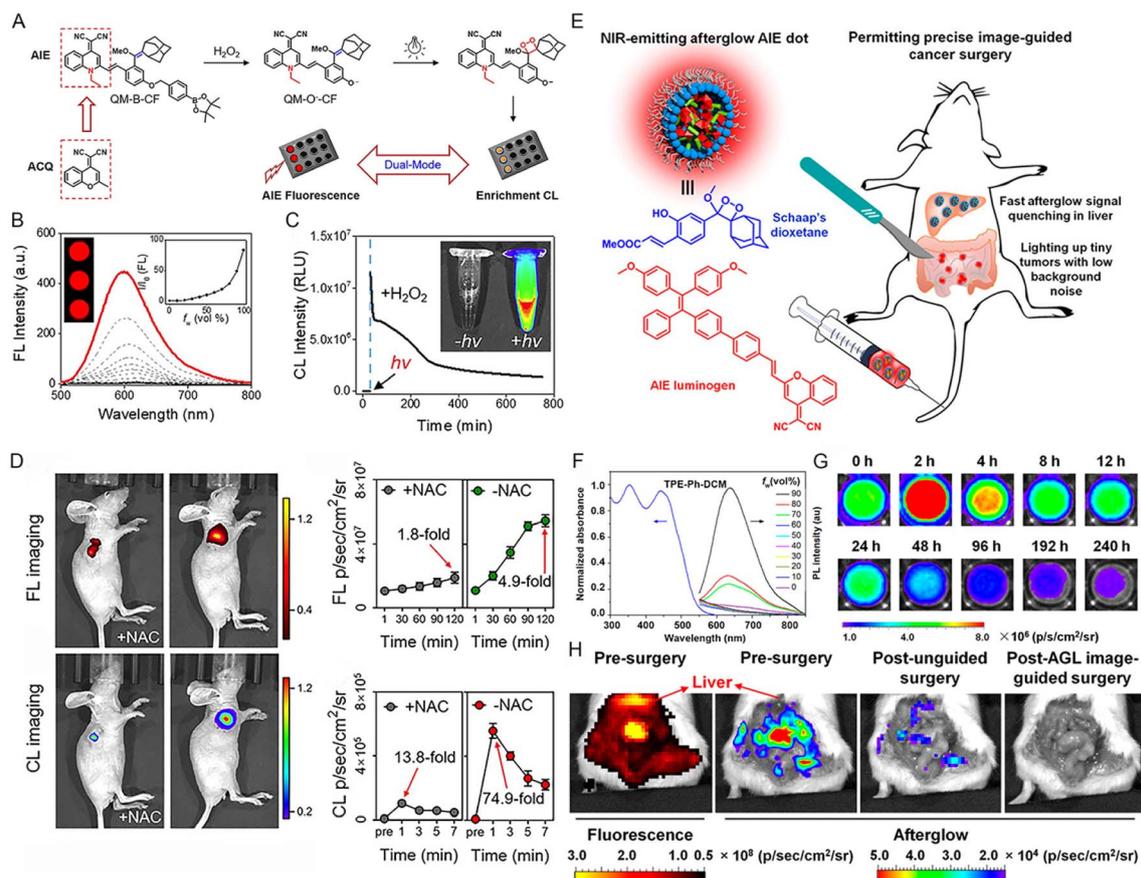
4860 | *J. Mater. Chem. A*, 2023, **11**, 4850–4875

This journal is © The Royal Society of Chemistry 2023

Fig. 10 (A) The rational design of the dual-lock strategy. (B) The emission spectra of the QM-O⁻-CF in PBS/DMSO mixture with various PBS buffer fractions. Inset: FL imaging of QM-O⁻-CF in the PBS/DMSO mixture with 99% PBS. (C) The time-dependent CL intensity of QM-B-CF in the presence of H_2O_2 after light irradiation (irradiation for 30 min). Inset: CL imaging of QM-B-CF (0.1 mM) treated with 1 mM H_2O_2 with or without light irradiation. (D) FL and CL imaging of xenograft 4T1 tumor-bearing mice after the intra-tumor injection of QM-B-CF with or without NAC. Reproduced with permission from ref. 113. Copyright 2020, Wiley-VCH. (E) Schematic illustration of NIR-emitting afterglow AIE dots and their outstanding performance in precise image-guided cancer therapy. (F) PL spectra of TPE-Ph-DCM (10 μM) in the THF/water mixture with different water fractions. (G) Time-dependent NIR afterglow of AGL AIE dots at 37 °C in PBS after 2 min pre-irradiated with white light (0.2 W cm⁻²). (H) The NIR fluorescence and afterglow imaging of the abdominal cavity before tumor surgery and typical afterglow images of the mice after unguided surgery and AGL image-guided surgery. Reproduced with permission from ref. 114. Copyright 2018, American Chemical Society.

addressing the bottleneck of CL technology in clinical detection.

It has been acknowledged that image-guided surgery is greatly beneficial for promoting the outcomes of cancer surgery in the clinic. Compared to photoluminescence, afterglow luminescence bearing far lower tissue background noise is emerging as a more-desirable modality for the intraoperative guidance of tumor resection. To this end, Ding's group[114] constructed a NIR afterglow luminescent nanoparticle (termed AGL AIE dots) through co-encapsulating AIEgen (TPE-Ph-DCM) and an enol ether precursor (compound 3) of Schaap's 1,2-dioxetane with lipid-PEG2000 (Fig. 10E). TPE-Ph-DCM exhibited an absorption range from 300 nm to 600 nm and a NIR emission spectrum, which was enhanced along with the increase of water fraction (f_w) (Fig. 10F). Besides, TPE-Ph-DCM also has favorable $^1O_2$ production capacity. Upon light irradiation, a series of processes including $^1O_2$ generation by TPE-Ph-DCM, Schaap's dioxetane formation, chemiexcitation by dioxetane

decomposition, and energy transfer to TPE-Ph-DCM would occur inside the AGL AIE dots, thus resulting in the NIR emission of TPE-Ph-DCM. Even after stopping the light irradiation, the NIR afterglow luminescence was able to persist for over 10 days (Fig. 10G). It has been demonstrated that the afterglow quenching rate of AGL AIE dots in the tumor was far slower than that in the main organs, thus resulting in a higher tumor-to-liver ratio (100-fold) of afterglow imaging than that of fluorescence imaging. Profiting from the ultrahigh tumor-to-liver signal ratio, as well as the low afterglow background noise, AGL AIE dots performed well in the precise image-guided cancer surgery. Most tumors, even minimal residual tumors with diameters less than 1 mm, can be resected.

In addition to tumor imaging, effective tumor eradication can be achieved by introducing AIE PSs as the energy acceptor in the CRET systems. In 2017, for the accurate diagnosis and therapy of tumors, Liu's group[115] developed a novel nanomaterial with far-red/near-infrared (FR/NIR) emission and $^1O_2$

This journal is © The Royal Society of Chemistry 2023

J. Mater. Chem. A, 2023, **11**, 4850–4875 | **4861**

production upon chemical excitation by co-encapsulating CPPO and an AIE PS (named TBD) to form C-TBD NPs. The obtained NPs can not only track tumors *in vivo* through chemiluminescence imaging but can also induce tumor cell apoptosis and inhibit tumor growth efficiently by the tumor H_2O_2-triggered $^1O_2$ generation.

3.4 Environmental monitoring

The spread and residue of chemically toxic, radioactive, and long half-life hazardous substances in the environment pose a major threat to human health and environmental protection, and the development of rapid, sensitive, and selective monitoring methods is critical.[116,117] Currently, AIE-active probes relying on chemical energy conversion represent promising tools owing to their unique aggregation-enhanced emission and high-emitting efficiency in the aggregate state or high concentrations.

For example, the uranyl ion (UO_2^{2+}), a stable form of core fuel uranium, is highly radio-hazardous.[116] In order to accurately monitor the UO_2^{2+}, Hua and coworkers[118] developed a "turn on" UO_2^{2+} probe based on ECL technology. The probe consisted of AIE-active polymer dots (Pdots), which were further modified with ssDNA (defined as DNA-Pdots) to capture UO_2^{2+} (Fig. 11A). The red shifted ECL spectra of DNA-Pdots with UO_2^{2+} as compared to that of DNA chains demonstrated the resonance energy transfer (RET) process between UO_2^{2+} and Pdots (Fig. 11B). Along with the gradual increase of UO_2^{2+} concentration from 0.05 to 100 nM, the ECL intensity was amplified (Fig. 11C). Compared to other interfering metal ions, UO_2^{2+} could provide notable signals even at deficient concentrations

(0.5 nM), confirming that the probe exhibited better sensitivity and selectivity for UO_2^{2+} ions (Fig. 11D). Benefitting from the amplified ECL signal of AIE-active Pdots based on the RET mechanism, the probe provided an ultralow limit of detection (LOD) (10.6 pM/2.5 ppt) of UO_2^{2+} (Fig. 11E). Accordingly, a portable ECL analyzer for the detection of UO_2^{2+} in natural water was constructed (Fig. 11F and G).

4 Mechanical energy conversion and applications

Mechanoresponsive luminescent (MRL) materials,[119–121] or mechanoluminescent (ML) materials,[122,123] whose luminescence behaviour changes in response to external pressure stimuli or other mechanical forces, represent an excellent platform for the utilization of mechanical energy in the luminescence field. Recently, many reported MRL or ML materials with AIE characteristics have attracted significant attention due to their unique mechanoresponsive capability and efficient emission in the solid state.[19,124,125] The highly twisted 3D conformation of AIEgens could significantly promote intermolecular anchoring in the crystal state, thus minimizing the energy loss caused by the slipping of molecules and finally improving the mechanical conversion efficiency.[126,127] On the other hand, the high sensitivity to an external perturbation can be obtained by triggering the loose packing of AIEgens, which could greatly reduce the molecular stacking strength in the solid state.[128] Thus, the twisted conformation and loose packing of AIEgens in the aggregate state are preferred in the design of AIE-active MRL or ML materials. Particularly, to reduce the background signal of AIEgens in the field of memory chips, the electron-rich groups are always introduced to improve the nonradiative ISC efficiency.[129] Due to the high contrast property and high force sensitivity, AIEgens with mechanoresponsive properties have been widely utilized in stress sensors, memory chips, health monitoring, and so forth.

4.1 Stress measurement

With the development of precise instruments and complicated structural components, structural health monitoring has become more and more critical and challenging in infrastructures[130,131] where the local stress/strain distribution of the materials is the most common factor. Compared to the conventional stress sensors based on the extensometers,[132] photoelastic principles,[133] and Raman spectroscopy,[134] the MRL stress sensors with visualized, real-time, full-field, and on-site monitoring have apparent advantages and are appealing for both academic research and industrial applications. Zou's group performed high-pressure studies on TPE and found that the emission of TPE would red-shift from 448 nm to 488 nm by gradually increasing the pressure to 10 GPa.[135] Such a large red-shift arises from the deformation of the C–H···π and C–H···C network associated with the amorphization process, which indicates the relevance between fluorescence efficiency and compression.
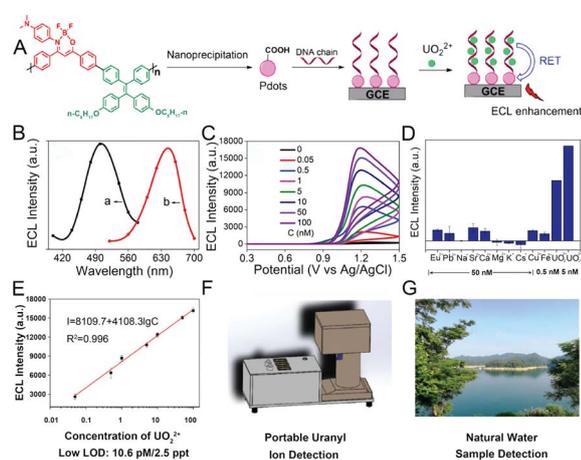

Fig. 11 (A) Schematic illustration showing the structure of the conjugated polymer, preparation of Pdots, and the mechanism of UO_2^{2+} detection. (B) The ECL spectra of UO_2^{2+} combined DNA chains (a) and UO_2^{2+} combined DNA–Pdots (b). (C) The ECL signals of Pdots in the presence of different concentrations of UO_2^{2+} in pH 7.4 PBS containing TPrA as a co-reactant. (D) The ECL signals of Pdots in the presence of different interfering ions, respectively. (E) Calibration curve of ECL intensity *versus* logarithm value of UO_2^{2+} concentration. Schematic illustration of the portable uranyl ion detector (F) and the natural water sample (G). Reproduced with permission from ref. 118. Copyright 2020, Wiley-VCH.

4862 | *J. Mater. Chem. A*, 2023, **11**, 4850–4875

This journal is © The Royal Society of Chemistry 2023

Tang and co-workers used a pure organic fluorophore named 1,1,2,2-tetrakis(4-nitrophenyl)ethane (TPE-4N) with obvious AIE activity to achieve the visualization of stress/strain distributions on metal specimens.[136] The TPE-4N was dispersed on the tensile specimen by dip-coating, then formed an amorphous TPE-4N film after air drying, and was finally crystallized by heating (Fig. 12A). The amorphous film showed strong green PL with an emission peak at 520 nm but the fluorescence was almost quenched in the crystal state due to the efficient ISC of the singlet state to the triplet state promoted by the nitro groups (Fig. 12B). The strain–fluorescence relationship of the TPE-4N-coated tensile specimen was performed on an imaging system that consisted of a coaxial

UV light, a CCD camera, an *in situ* fatigue testing machine, and a computer for analysis (Fig. 12C). When a force was applied, green luminescence was observed and enhanced gradually with increasing strain (ε, %) in real-time (Fig. 12D). To quantitatively assess stress, the fluorescence of a selected area in the middle was analyzed by image software in which each pixel was calculated to represent the intensity of the fluorescence signal (Fig. 12E). The strain-grayscale curve showed the same trend as the strain–stress curve of stainless steel (Fig. 12F), suggesting that the fluorescent signal of the TPE-4N coating can be used to clearly visualize the stress accumulation during strain loading, which further predicts the pathway of fatigue crack propagation in advance.
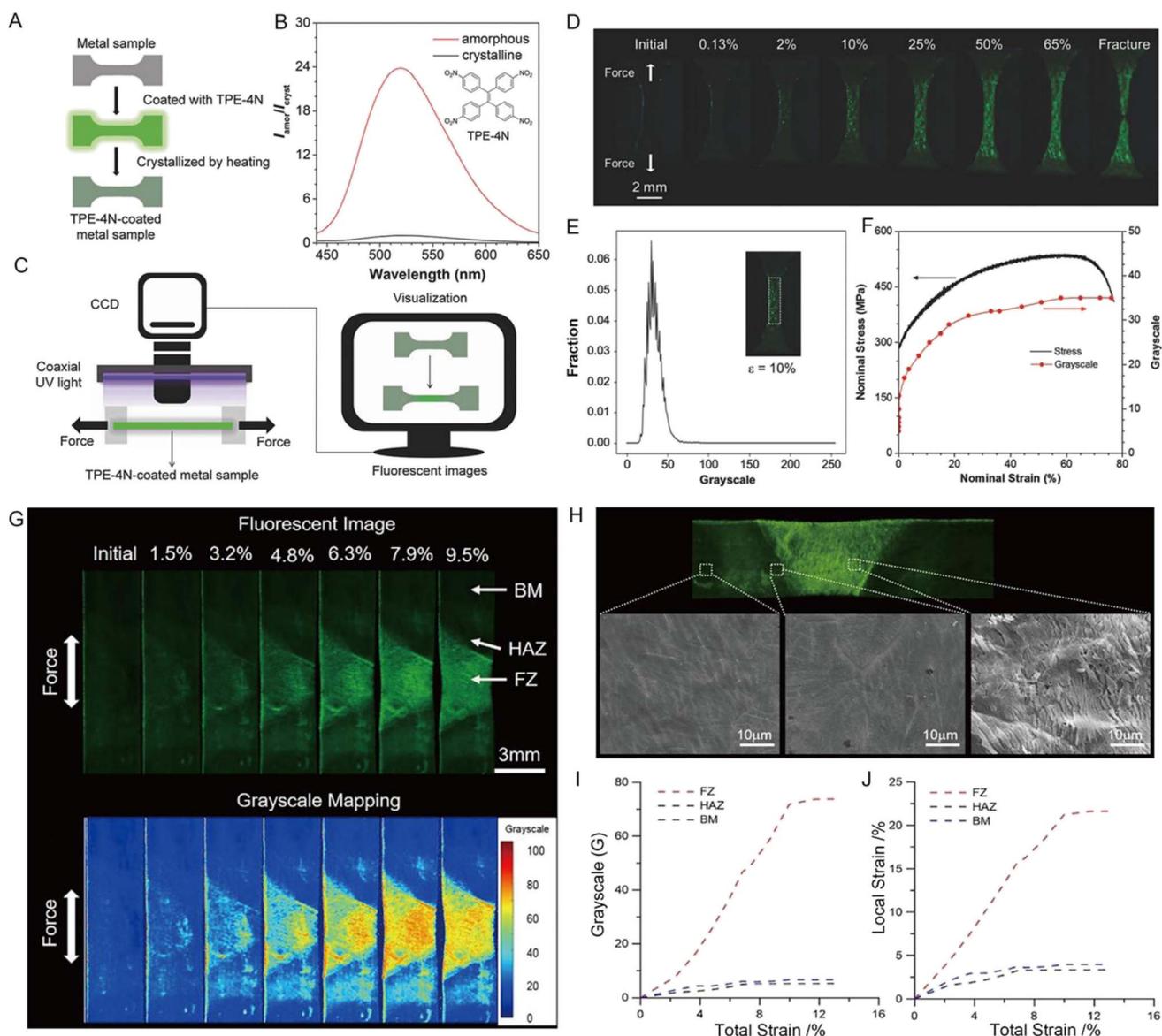
Fig. 12 (A) Illustration of sample preparation of the TPE-4N-coated metal specimen. (B) PL spectra of TPE-4N film in amorphous and crystalline states. (C) Illustration of the experiment setup. (D) Fluorescence images of the TPE-4N-coated steel tensile specimen at different strains (ε, %). (E) Gray-scale distribution of the selected area at $\varepsilon = 10\%$. (F) Plots of strain against stress and gray-scale of the TPE-4N-coated steel tensile specimen. Reproduced with permission from ref. 136. Copyright 2018, Wiley-VCH. (G) Fluorescent and gray-scale mapping of tensile results of the weld joint. (H) Morphology of TPE-4N film on the surface of the stretched weld joint specimen. (I) Local gray-scale variation and (J) calculated local strain in different regions. Reproduced with permission from ref. 137. Copyright 2020, American Chemical Society.

This journal is © The Royal Society of Chemistry 2023

J. Mater. Chem. A, 2023, **11**, 4850–4875 | **4863**

Based on the excellent MRL properties of TPE-4N between amorphous and crystalline states, Tang and co-workers further demonstrated the versatility of TPE-4N in the structural health monitoring of weld joints, which is usually more vulnerable to in-service repetitive and fluctuating loading.[137] The fluorescence and gray intensity in the weld joint were inhomogeneous during monotonic tensile deformation, and the inhomogeneity grew with increasing total strain (Fig. 12G). Three regions of the weld joint, known as the base material (BM), fusion zone (FZ), and heat-affected zone (HAZ), can be identified well *via* visual fluorescence (Fig. 12H). The variation tendency in the total strain-grayscale curve (Fig. 12I) of each part was the same as that of the total strain-local strain curve (Fig. 12J), indicating the accuracy of visualization results. The organic MRL method opens up new opportunities for large-scale, full-field, and real-time visualization for local strain concentration, which will be beneficial for early damage detection in aeronautics, astronautics, and automobile industries.

4.2 Information storage

The photoluminescence properties of AIE-active MRL materials are susceptible to external forces and can store information or data on the material through mechanical stimuli such as grinding, ball milling, and crushing. In addition, fluorescence emission and color changes can be recovered by various stimuli such as heating, organic solvent vapor, and light. The high contrast of "on–off" properties and stress sensitivity are the most significant factors for the "smart memory materials". Some studies used the processes of photodimerization,[138] intramolecular charge transfer,[139] and strong π–π interaction modulation[140,141] to reduce the initial luminescence of the crystal state. However, the solid intermolecular interactions require strong forces to induce the evident morphology or conformation switching and restrict the photophysical processes of the excited state.

To realize high contrast on–off luminescence switching in the presence of a small mechanical stimulus, Tang and coworkers proposed a new design strategy for highly sensitive MRL materials based on the control of the ISC process by using a nitrophenyl group.[142] A lone pair from the electron-rich nitrophenyl group with a tremendous spin–orbit coupling constant and negligible energy gap (ΔE_{S-T}) can boost the efficient ISC pathway. On the other hand, the morphology of the AIEgen with a twisted conformation can be easily modulated by mechanical stimulus. The freshly TPE-4N coated film is quite transparent and smooth with bright green light at 520 nm, and the emission was
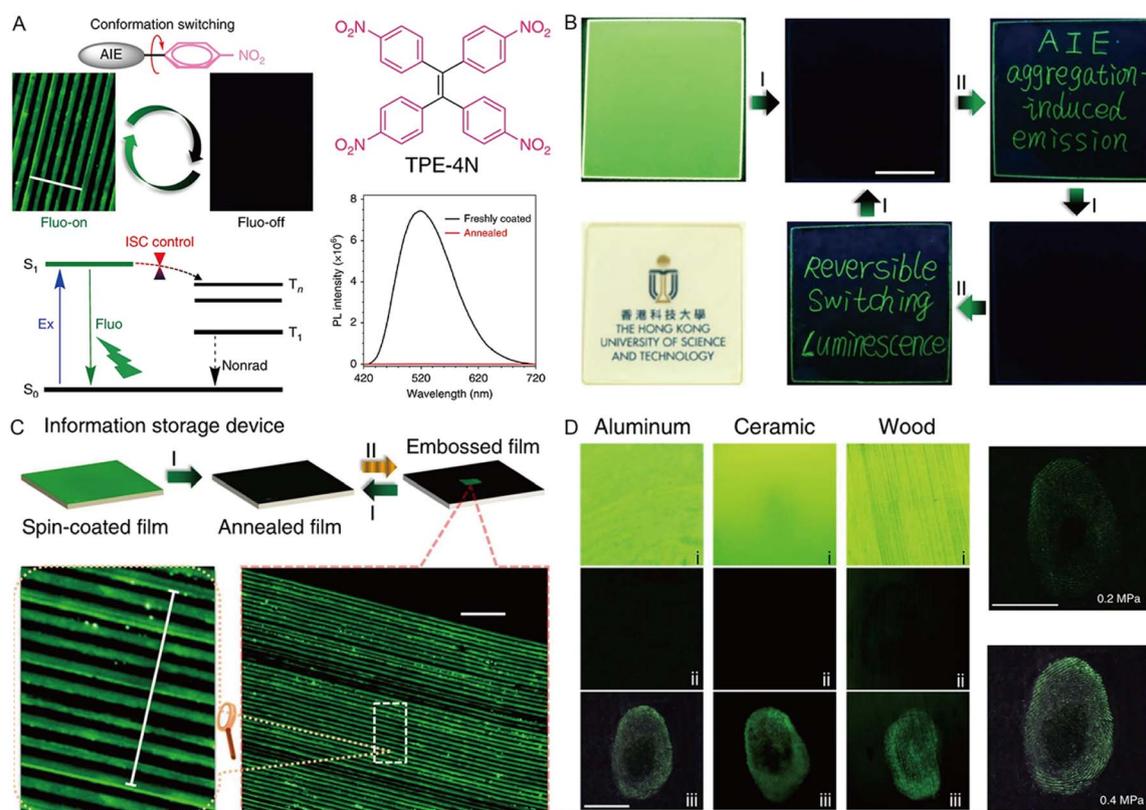

Fig. 13 (A) Proposed mechanism for highly sensitive "on–off" MRL materials by controlling the intersystem crossing of TPE-4N. Scale = 100 μm. (B) Luminescent and room-light transparent photos of the TPE-4N thin-film spin-coated on a quartz plate and records of the writing and erasing processes. (C) Procedures for the micro-embossing and recovery on the thin film of TPE-4N prepared by spin-coating, and luminescent photos of micro-embossed patterns. (D) Haptic photos of fingerprints on aluminum, ceramic, and wooden substrates coated with TPE-4N, including freshly brush-coated film (i), annealed film (ii), and film pressed with a finger (iii). Reproduced with permission from ref. 142. Copyright 2018, Nature Publishing Group.

4864 | *J. Mater. Chem. A*, 2023, **11**, 4850–4875

This journal is © The Royal Society of Chemistry 2023

quenched quickly when the film was annealed at 150 °C (crystalline state), indicating the fluorescence quenching *via* a non-radiative ISC channel by nitrophenyl groups (Fig. 13A). Well-defined and bright green emissive words appeared when writing on the annealed film using a fine glass tube. After thermal treatment, the emissive words were erased completely (Fig. 13B). The writing and erasing processes can be repeated many times, suggesting the excellent reversibility of the fluorescence switching process. The rewriteable optical information storage system showed micro-embossed fluorescent patterns with a width of 10 μm and a spacing of 10 μm (Fig. 13C). The micrometer resolution of the system made it possible to construct haptic sensors to store the fingerprint, and various substrates such as aluminum, ceramic, and wood can all be used by a simple brush coating process (Fig. 13D), suggesting a promising fast-responsive and reversible haptic sensor.

4.3 Health care

ML materials with high force sensitivity have great potential to monitor the mechanical properties of the local environment and the human body,[143,144] and the luminescence converted from the external mechanical energy is a sensitive and visible responsive signal providing valuable insights into the artificially intelligent systems and human health status.[145,146]

Li and coworkers[147] developed an ML-induced health monitoring device using TPE-2-Th, of which TPE was chosen as the skeleton to ensure the AIE features, while a thiophene (Th) unit was introduced onto the TPE core for the adjustment of molecular packing in the crystal state. TPE-2-Th showed sensitive and stable ML performance due to the lower potential energy barriers, which facilitated more persistent ML emission and tight packing owing to the strong C–H⋯S interactions between adjacent molecules under continuous force. In the ML device, TPE-2-Th crystals were sandwiched by polymeric ethylene-vinyl acetate copolymer (EVA) layers to act as the ML-emitting material (Fig. 14B). The experimental setup for testing the quantitative relationship between pressure force and ML intensity is shown in Fig. 14A. The ML intensity of the device became more robust with the increase in pressure. In contrast, the maximum intensity of 1400 under the pressure of 14 N could be defined as the limiting value of the device (Fig. 14C). ML intensity at 460 nm with the corresponding pressure from 0 to 17 N was fitted, which exhibited a standard linear function (slope = 17.00, adjusted $R^2 = 0.967$) at a pressure ranging from 0–6 N and a single exponential function (adjusted $R^2 = 0.983$) from 6–14 N (Fig. 14D). Based on the definite quantitative relationship between pressure and ML intensity, some simple wearable devices were fabricated for the application of impact strength warning and heartbeat detection (Fig. 14E and F). The pressure applied on the device could be converted into light with corresponding intensity, and the thresholds of the warning signal could be redefined according to different conditions such as external force to the joint and heart rate. In this way, the elusive heartbeat and external force on the joint can be converted into a type of light signal with convenience, warning, and visualization characteristics.
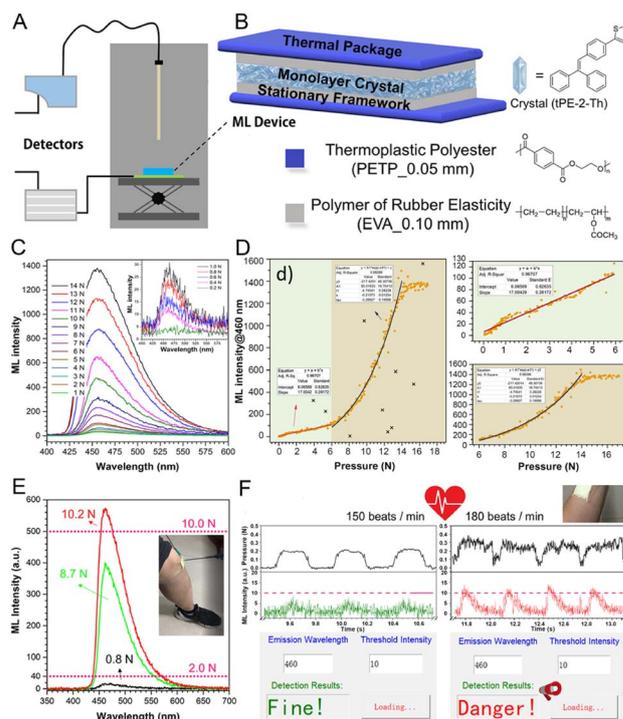

Fig. 14 (A) Experimental setup for testing the quantitative relationship between pressure force and ML intensity. (B) Schematic structure of ML devices (*t*PE-2-Th). (C) The ML spectra under different pressure forces derived from a type-A device (with large-sized crystals). (D) Quantitative relationship of the type-A device (ML intensity at 460 nm). (E) Schematic diagram of wearable devices in the application of impact strength warning. (F) Schematic diagram showing heartbeat detection and warning behavior. Reproduced with permission from ref. 147. Copyright 2020, Cell Press.

The ML materials in the crystal state are usually crisp and the fracture caused by the external force is irreversible, which greatly hampered their biomedical applications. Soft materials with easy and reversible deformation properties were desired to promote the flexibility of ML materials.[125] Chi and co-workers designed[148] the TPE-based hydrogen-bonded organic frameworks (HOFs) with permanent porosity exhibiting outstanding luminescence properties. Due to the weak hydrogen bonds, the ML HOFs show more soft, poorly directional, and recoverable deformations, thus resulting in the reversible ML property, shape flexible and easy fabrication of biomedical devices.

5 Electric energy conversion and applications

Optoelectronic devices are a significant component of optoelectronic technology that can convert energy from electrical to optical or optical-to-electrical.[149] In photoelectronic areas, light-emitting materials are commonly utilized in the solid state, where the AIEgens present significant advantages.[18,150] The unique twisted structure of AIEgens prevents the fluorescence quenching caused by the intermolecular π–π stacking in close packing conditions,[151] especially in the solid or crystal state,

This journal is © The Royal Society of Chemistry 2023

J. Mater. Chem. A, 2023, **11**, 4850–4875 | **4865**

increasing the energy conversion efficiency of optoelectronic devices. Moreover, the excellent thermal and morphological stabilities,[152] flexible design strategy[18,23] and resistance to photobleaching[153] and photoaging[154] of AIEgens promote optoelectronic applications in the fields of organic light-emitting diodes (OLEDs), organic field-effect transistors (OFETs), liquid crystals (LCs), and solar cells.

5.1 Organic light-emitting diodes (OLEDs)

OLEDs have exhibited great commercial applications in display devices and solid-state lighting sources due to their advantages of low power consumption, flexibility, high efficiency, ultrahigh contrast ratio, and good purity.[155,156] In the electroluminescence (EL) process, light is produced by recombining holes and electrons in the light-emitter layer of OLED devices.[157] Therefore, high luminescence efficiency and increased exciton utilization are crucial to achieving the high performance of OLEDs. However, the emissive layer is usually weakly emissive in the solid state due to the effective dipole–dipole interactions and intermolecular π-stacking. The aggregation-caused quenching (ACQ) effect has severely hindered the practical application.[158,159]

Compared to non-AIE compounds, the AIE compounds have a spatial distorted molecular structure to prevent compact molecular interactions in the aggregated state. However, the distorted structure of materials may hamper the charge transport, resulting in low carrier mobility, and the orbital energy level could also affect energy conversion in the emissive layer.[160] Thus, to further improve the EL performance, some molecular design strategies are usually adopted, such as adding weak binding among molecules to reduce the non-radiative transitions, or introducing polycyclic aromatic hydrocarbons to promote carrier mobility. For example, Tang and coworkers[161] developed a novel multifunctional AIEgen (SBF-BP-DMAC) as shown in Fig. 15A, and the molecular packing mode of SBF-BP-DMAC in the crystal displayed a highly twisted conformation and multiple weak interactions, thus alleviating nonradiative energy loss and enhancing emission efficiency in the solid state (Fig. 15B). The SBF-BP-DMAC neat film displayed a high photoluminescence QY of 72.1%. By combining the emission behavior of SBF-BP-DMAC in THF/water binary solutions, SBF-BP-DMAC showed typical aggregation-enhanced emission (AEE) character and promoted delayed fluorescence in the solid state and bipolar carrier transport ability (Fig. 15C). Further, SBF-BP-DMAC was used as a host to prepare the light emitter in the non-doped and doped forms of OLEDs with excellent performances. The non-doped OLEDs (device G1) exhibited maximum EL efficiencies of 31 206 cd m^{-2}, 67.2 cd A^{-1}, 65.9 lm W^{-1}, and 20.1%, respectively, demonstrating the high utilization efficiency of electrogenerated excitons (Fig. 15D and E). Furthermore, the doped devices O1–O3 showed maximum luminance from 111 772 to 145 605 cd m^{-2}, confirming the high luminescence efficiency, and sufficient energy transfer from the host to the guest was achieved (Fig. 15F and G). This work verified that the high exciton utilization efficiency based on AIEgens is conducive to achieving a high EL efficiency.

To achieve higher electron mobility and good light-emitting properties, the researchers focused on large p-conjugated polycyclic aromatic hydrocarbons such as pyrene.[162,163] However, pyrene exhibits fluorescence quenching with a low QY in the solid state due to the large planar structure.[164] To obtain pyrene-based OLEDs devices with high performance, Tang and coworkers reported a series of Y-shaped pyrene-cored emitters decorated with either TPA or TPE units (Fig. 15H).[165] The emission behaviors of Py-TPA and Py-2TPE compounds not only presented high luminous efficiencies (Fig. 15I) but also proved their AIE features (Fig. 15J). 4,4′-Bis(N-carbazolyl)-1,1′-biphenyl (CBP) doped with 10 wt% of guest Py-TPA or Py-2TPE was used as the light emitting layer (Fig. 15K). The doped devices Py-TPA and Py-2TPE exhibited excellent electroluminescence emission with a low turn-on voltage of 2.9 V (Fig. 15L), a maximum external quantum efficiency of 7.27% (Fig. 15M), and high exciton utilization efficiency of 77.3%. These important results will be helpful for the design of a more efficient AIE-based emitter layer with high external quantum efficiency (EQE) and provide a new strategy for preparing high-performance OLEDs by efficiently utilizing the higher energy excitons.

White-light OLEDs are attractive due to their low energy consumption, high efficiency, and long lifetimes. The AIE-based scaffolds provided a novel strategy for achieving the single-source white-light emission materials from complementary colors.[166–168] Li et al.[169] employed the 1,1,2,2-tetrakis(4-(pyridin-4-yl)phenyl)-ethene (TPPE) ligand zinc-based metal–organic framework (MOF) to tune the HOMO–LUMO energy gap, and finally achieved the blue-excitable yellow-emitting property with 90.7% internal quantum yield. The high photo-stability was rarely observed in pure organic white-light OLEDs; hence, Wang and co-workers[170] designed TPE-based 3D COFs, which exhibited no degradation after aging for 1200 h under ambient conditions.

5.2 Organic field-effect transistors (OFETs)

OFETs have displayed critical importance in developing advanced flexible optoelectronic devices.[171,172] However, developing materials with high charge mobility and strong luminescence is still a significant challenge. For organic electronics, intermolecular π–π interactions usually arise within n-type semiconductors with electron-deficient characteristics to form conducting pathways.[173,174] However, intermolecular π–π stacking is detrimental to emission efficiency because of the generation of excimers or exciplexes. To overcome the ACQ problem, AIEgens with high emission efficiency exhibit distinct advantages for practical applications in the OFETs field. Although AIE-active materials have high luminescence properties, the carrier mobility of the previously reported AIEgens is very low due to the distorted molecular conformation and weak π–π stacking in the solid. Previously, it was proved that ACQ molecules could be transformed into AIE molecules by decorating with AIE building blocks, such as TPE units in the bay area of the PDI core[175] but the highly twisted structure of the TPE unit would inhibit effective charge transport. Tang and coworkers designed a series of perylenediimide (PDI)-
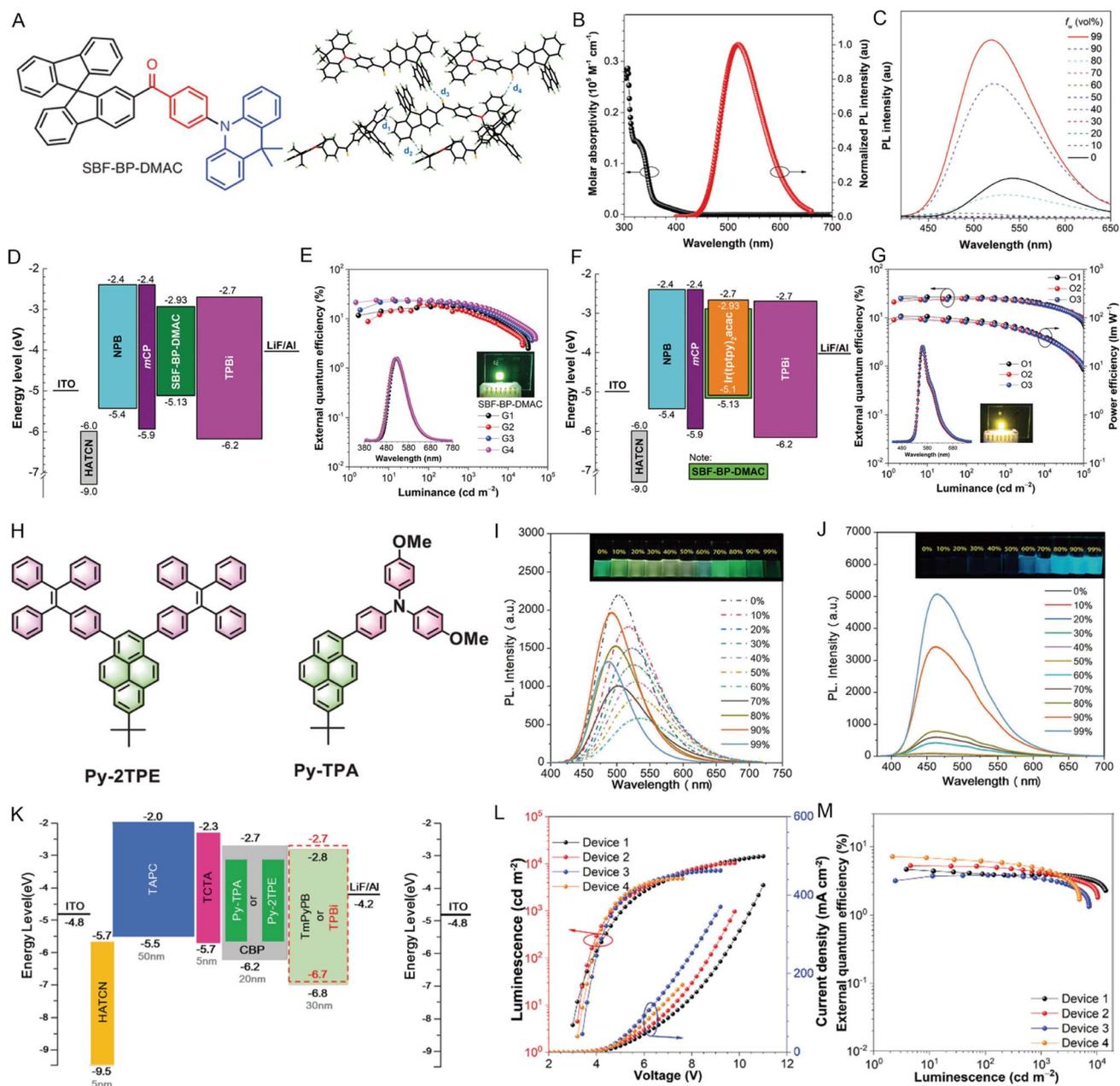
4866 | J. Mater. Chem. A, 2023, **11**, 4850–4875

This journal is © The Royal Society of Chemistry 2023

Fig. 15 (A) Chemical structure of SBF-BP-DMAC. Packing pattern and intermolecular interactions of SBF-BP-DMAC in crystals. (B) Absorption spectrum of SBF-BP-DMAC in THF solution (10 μM) and the normalized PL spectrum of the SBF-BP-DMAC neat film. (C) PL spectra of SBF-BP-DMAC in THF/water binary solutions with different water fractions. (D) Device structures and energy diagrams of the non-doped device. (E) Plots of external quantum efficiency of devices G1–G4. (F) Device structures and energy diagrams of the doped device. (G) Plots of external quantum efficiency characteristics of devices O1–O3. Reproduced with permission from ref. 161. Copyright 2020, Wiley-VCH. (H) The designed pyrene-based molecules Py-TPA and Py-2TPE. PL spectra of (I) Py-TPA and (J) Py-2TPE in THF/water mixtures with different water fractions. (K) Device structures and energy diagrams of doped devices. (L) Luminance–voltage–current density (L–V–J) characteristics of the OLED devices. (M) Plots of external quantum efficiency of the OLED devices. Reproduced with permission from ref. 165. Copyright 2022, Wiley-VCH.

substituted triphenylethylenes (TriPE-nPDIs (n = 1–3)).[176] The study showed that selecting appropriate TriPE units with balanced molecular planarity and incorporating large π-conjugated units into the AIE framework enhanced the intermolecular interaction and promoted charge transport (Fig. 16A). The emission property of TriPE-nPDIS was studied in chloroform/hexane mixture solutions, suggesting that they are AEE-active

(Fig. 16B). These compounds displayed n-channel charge-transport properties, and by increasing the PDI number, the charge mobility trends were also increased. The AIEgens with more PDI units and moderate twisting conformations could promote both strong emission and charge transport, along with the maximum QY reaching about 30% and optimized electron mobility exceeding 0.01 cm^2 V^{-1} s^{-1} (Fig. 16C and D). The

This journal is © The Royal Society of Chemistry 2023

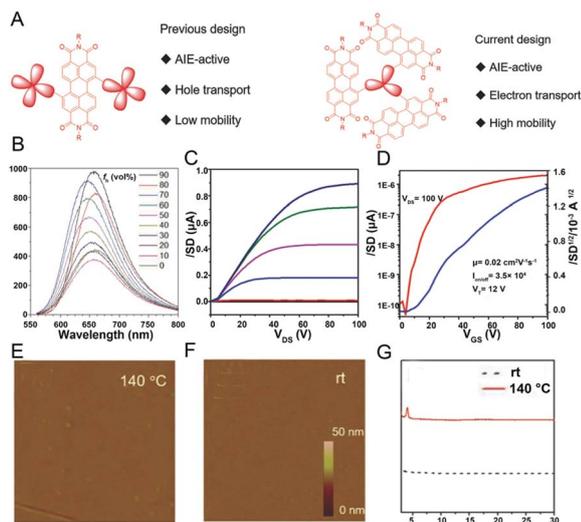J. Mater. Chem. A, 2023, 11, 4850–4875 | 4867

Fig. 16 (A) The design principles of AIEgen-based OFET devices. (B) TriPE-3PDI in CHCl$_3$/hexane mixtures with different hexane fractions (f_h). (C) Transfer and (D) output characteristics for OTFT devices of TriPE-3PDIL annealed at 140 °C. AFM images of TriPE-3PD at (E) 140 °C and (F) at room temperature. (G) XRD patterns of thin films of TriPE-3PDIL at room temperature and 140 °C. Reproduced with permission from ref. 176. Copyright 2018, Wiley-VCH.

atomic force microscopy (AFM) and X-ray diffraction (XRD) (2θ = 4.06°) of thin films of TriPE-3PDI suggested that the enlargement of the molecular π-conjugation of AIEgens in the OFET device was effective for enhancing charge mobility (Fig. 16E and F), and the crystallinity of films also played an essential role in charge transport (Fig. 16G). The results demonstrated the great potential of AIEgens in organic OFET emitters.

5.3 Liquid crystals

Liquid crystals (LCs), as an intermediate phase between a solid crystal and an isotropic fluid with advantages of simple device configuration, low energy consumption, and high information density,[177] have been widely used in the fields of polarized organic lasers,[178] anisotropic OLEDs,[179] and liquid-crystal displays (LCDs).[180] However, conventional LCs are mostly non-emissive, which leads to unpolarized backlight as well as low brightness and poor energy efficiency of the corresponding optical displays. In order to address the problem, some light-emitting molecules were doped into the LCs to enhance the luminescence brightness and efficiency of energy conversion.[181,182] However, there are still some challenges for such materials in molecular design and emission quenching in the crystal state.[183,184] Fortunately, AIEgens exhibit intensive fluorescence at the aggregate state, differing from the ACQ effect, due to the twisted conformation of AIE molecules. Thus, employing AIEgens in LCs represents an effective method for enhancing the optical performance of LC materials. To be specific, after flexible alkoxy groups were attached, the obtained AIEgens could easily form LCs. Besides, strategies that dope AIEgens into formed chiral nematic LCs and assemble the

AIEgens as templates for the binding of LCs have also been widely reported.[185–187]

The attachment of flexible alkoxy groups to the rigid AIE-active core is an effective construction strategy for AIE-active LCs. Tang and coworkers designed the TPE-based molecule TPE-PPE consisting of four mesogenic units with alkyl chains and a TPE core in which the mesogenic properties ensure miscibility and anisotropy of the mix with nematic LC.[188] The TPE-PPE exhibited thermotropic disc SmC phase behavior as well as luminescence properties. As mentioned above, by decorating the AIE cores with long alkyl/alkoxy chains, diverse AIE-based mesogens could be easily fabricated to create new LCs with modulated emission properties.[185,186,189] Another strategy could also be achieved by doping AIEgens into formed chiral nematic LCs. Cheng's groups prepared chiral nematic liquid crystals (N*-LCs) by mixing chiral binaphthyl molecules (guest 1) into nematic liquid crystals (N-LCs), then AIE-N*-LCs were prepared by introducing four achiral AIE dyes (guest 2) into N*-LCs (Fig. 17A). N*-LCs exhibited liquid crystallinity and typical fingerprint textures, indicating the good compatibility of chiral dopant guest 1 with N-LC and the regular characteristic fingerprint texture of the AIE-N*-LCs could be observed by doping achiral Guest 2 into the above N*-LCs (Fig. 17B). The strong circularly polarized luminescence (CPL) signals could be greatly promoted *via* the assembly of N*-LCs, and their emission wavelength could be tuned by doping various AIE-active dyes, providing a novel strategy for developing LCs with excellent CPL.[190]

AIEgens not only act as dopants but also form the chiral nematic LC phase *via* chiral amplification.[191] Recently, Tang and coworkers reported a chiral AIE molecule/LCs supramolecular system[192] in which four chiral AIE molecules (Fig. 17C) were self-assembled into helical fibers following a "sergeant and soldier" rule[193] to serve as the helical template for the binding of LCs (4-cyano-4′-phenylbiphenyl, 5CB) (Fig. 17D). Theoretical calculations further provided more detailed information on how the molecular packings and interactions led to the formation of different co-assemblies with 5CB (Fig. 17E). The pure 5CB exhibited a Schlieren texture and typical cholesteric fingerprint textures were formed by gradually increasing the ratio of *p*-TPE-NC, and the helical pitch decreased with the increasing doping ratio indicating the co-assembly of helical TPE derivatives with 5CB (Fig. 17F and I). In general, the chiral amplification of AIEgens provided a potential strategy for fabricating the LC materials with a defined structure at the nanoscale.

5.4 Solar cells

Solar cells are expected to represent the next generation of clean energy with the advantages of low cost, simple processing, infinite energy source, large area printing, and flexible substrates.[194–196] The energy conversion efficiency is a critical factor of solar cells, which has been improved tremendously from the initial 3.8% to above 24% over the last several years owing to the improvement of film quality and device architectures, as well as the exploitation of new donors and
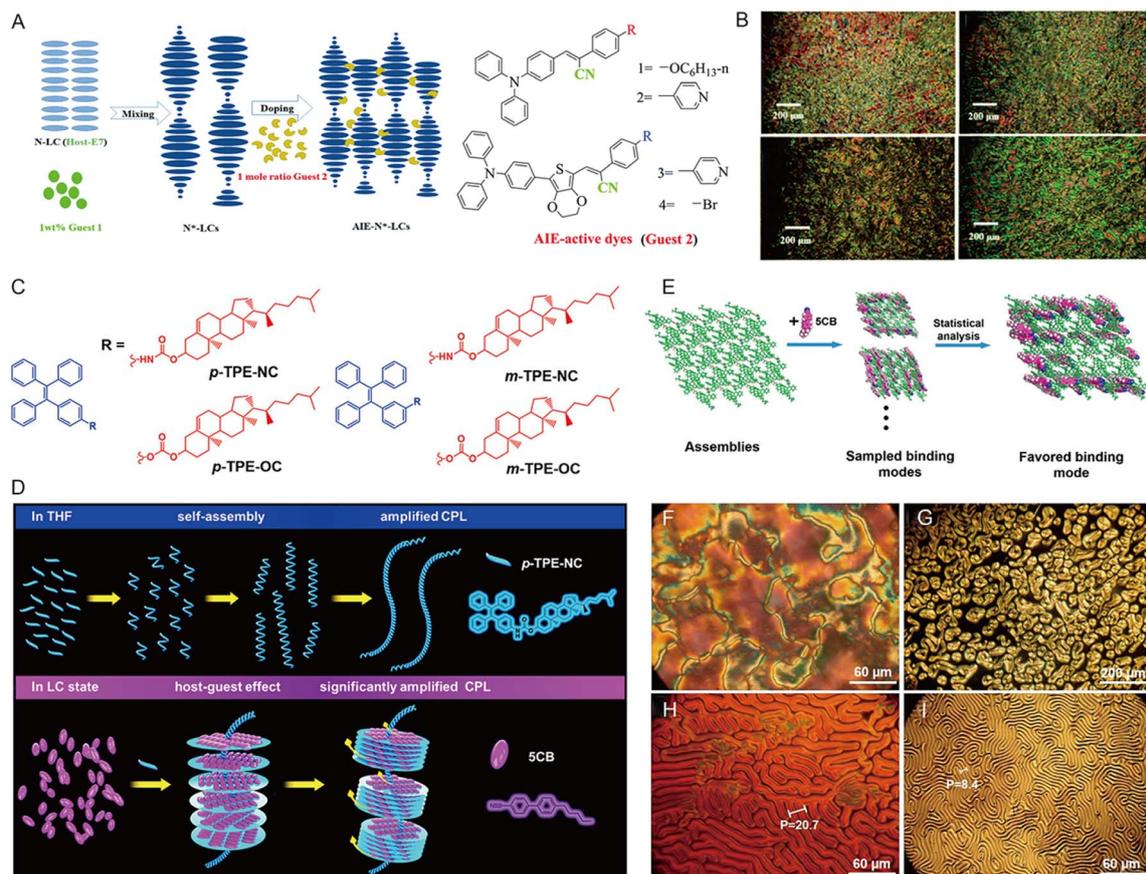
4868 | *J. Mater. Chem. A*, 2023, **11**, 4850–4875

This journal is © The Royal Society of Chemistry 2023

Fig. 17 (A) The structural formulae of AIE dyes and the schematic diagram of the AIE–N*–LC assembly. (B) AIE–N*–LCs doped with 1 wt% R-guest 1 and the 1 mole ratio of the AIE-active dyes (guests 2–1, 2, 3, and 4) in flat LC cells at 25 °C. Reproduced with permission from ref. 190. Copyright 2019, Royal Society of Chemistry. (C) TPE derivatives bearing cholesterol attachments. (D) Illustration of the chiral amplification of TPE derivatives containing cholesterol attachments in LCs. Helical assemblies of TPE derivatives are located in the axes of the co-assemblies serving as helical templates for LC molecules to bind. (E) The favored binding mode between 5CB molecules and modeled assemblies. POM images of 5CB doped with *p*-TPE-NC on untreated glass slides: (F) 0 wt%, (G) 0.1 wt%, (H) 0.5 wt%, (I) 1 wt%. Reproduced with permission from ref. 192. Copyright 2021, American Chemical Society.

acceptors.[197–200] In the standard structure of the solar cells, the organic molecules were usually used as hole-transport materials (HTMs), which promoted the separation of holes from the perovskite layer and simultaneously transported them to the top metal anode.[201–203] One of the significant factors of HTMs in solar cells is high charge mobility (high nonradiative decay rate, k_{nr}) in the solid state. In this respect, the AIEgens with twisted molecular conformation could be designed to increase the k_{nr} by reducing the intermolecular π–π stacking and restricting the intramolecular motions in the aggregate state. On the other hand, the AIEgens with low HOMO energy levels could also be designed to improve the hole transfer from perovskite to HTMs. Hence, HTMs with AIE properties might be promising as charge transport candidates.[204,205] He and co-workers developed an organic AIE molecule of 2-(2,7-bis(4-(bis(4-methoxyphenyl)amino)phenyl)-9H-fluoren 9ylidene)malononitrile (TFM)[206] (Fig. 18B) as HTMs in the inverted planar perovskite solar cells (PSCs), obtaining the optimal power conversion efficiency of 16.03% (Fig. 18A). Ultraviolet (UV) photoelectron spectroscopy (UPS) demonstrated that the HOMO energy level was about

−5.45 eV for TFM film, which was lower than the commonly used PEDOT:PSS HTM, indicating the enhancement of hole transfer from perovskite to HTMs (Fig. 18C). The device with TFM had excellent photovoltaic performance with higher short-circuit current density (J_{sc}) and open-circuit voltage (V_{oc}) (Fig. 18D). Moreover, the TFM-based devices exhibited better EQE response over the whole visible spectrum when compared with the PEDOT:PSS-based devices (Fig. 18E). Similarly, Chen's group[194] reported a low-cost and efficient AIE-active HTM TPE-CZ based on a TPE core and the *p*-methoxydiphenylamine-substituted carbazole (CZ) functional group, achieving the excellent power conversion efficiency of 18% and much better stability than the reference AIE-free HTMs.

In addition to power conversion efficiency, photostability, especially ultraviolet stability, is the main limitation in practical applications.[207,208] The devices based on the ZnO electron transport layer (ETL) with poor UV light stability would undergo the degradation of the device under UV conditions. To improve device photostability, Chen's group presented an efficient strategy for enhancing the UV stability of solar cells *via* coating
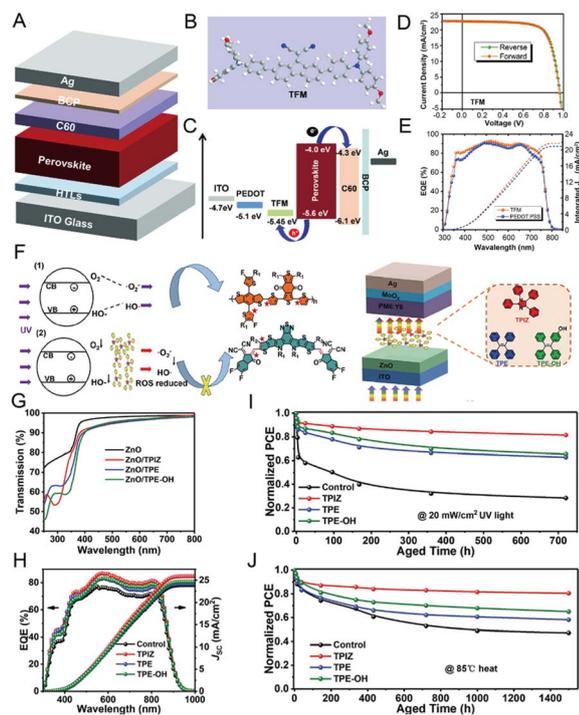
This journal is © The Royal Society of Chemistry 2023

J. Mater. Chem. A, 2023, **11**, 4850–4875 | **4869**

Fig. 18 (A) Diagram showing the device architecture used in the present work. (B) Molecular structure of the TFM HTM. (C) Energy-level alignment of different layers in the device. (D) Current−voltage curves of the optimal inverted PSCs with TFM. (E) EQE spectra of the optimal inverted PSCs with TFM and PEDOT: PSS HTMs. Reproduced with permission from ref. 206. Copyright 2019, Wiley-VCH. (F) The mechanism scheme for improving the UV light stability of devices by the AIE barrier layer and the chemical structures of the polymer donor PM6, acceptor Y6 and three kinds of AIE molecules. (G) Transmission spectra of ZnO and ZnO/"AIE" films. (H) The corresponding EQE characteristics of PM6:Y6 OSCs with ZnO and ZnO/"AIE" interfacial layers under simulated AM 1.5 G irradiation (100 mW cm^{-2}). PCE decay of PM6:Y6 devices based on ZnO and ZnO/"AIE" (I) under continuous UV illumination (365 nm, 20 mW cm^{-2}), (J) under continuous annealing at 85 °C. Reproduced with permission from ref. 194. Copyright 2022, Wiley-VCH.

an AIE molecular optical barrier layer between the interface layer and the active layer.[209] Three representative AIE molecules based on 1,2,3,5-tetraphenylimidazole (TPIZ), TPE, and 4-hydroxytetraphenylene (TPE-OH) were used to evaluate the impact of the photoresist layer (Fig. 18F). From the transmission spectra of ZnO and ZnO/"AIE" in Fig. 18G, the AIE-based layer reduced the UV transmission from 80.13% to 59.21%. On the other hand, the J_{sc} and EQE were both increased in AIE groups (Fig. 18H and J), and with ZnO/TPIZ as the ETL, the highest power conversion efficiency increased from 15.04% (ZnO) to 16.37%. The AIE layer showed both excellent UV resistance and thermostability over a long period of aging time, especially the TPIZ-based layer. The introduced AIEgens absorbed UV light and emitted visible light, which overlapped with the absorption peak and broadened the spectral range, not only improving the photostability of ETL but also improving the electron extraction performance and inhibiting charge

recombination by enlarging the power conversion efficiency of the devices.

6 Conclusions and outlook

Benefiting from the unique optical properties, twisted molecular configuration, diverse structures, easy tailorability, and modification flexibility, it is technologically convenient to modulate or equilibrate the energy dissipation channels of excited AIEgens as required by tactically adjusting the aggregation state as well as the intramolecular motions of AIEgens. This enables AIEgens to be ideal platforms for achieving diverse energy transformation as well as various applications. For the first time, we have outlined the recent advancements of AIEgens from the viewpoint of energy transformation. Specifically, this review showcases in detail the solar energy transformation-based applications in wound healing, PPE, water governance, thermal insulation and photosynthesis, chemical energy conversion-related applications in biomarkers detection, inflammation imaging, tumor imaging, surgical guidance and environmental monitoring, mechanical energy transformation-involved applications in stress measurement, information storage and health care, as well as electrical energy conversion-dependent applications in OLEDs, OFETs, liquid crystals, and solar cells.

The excellent progress in diverse energy transformation has validated the great potential of AIEgens in enhancing energy utilization efficiency when facing the severe challenge of a global energy shortage; however, there are still some challenges, or perhaps opportunities, that should be mentioned in the pursuit of improving the energy conversion efficiency of AIEgens as well as boosting the utilization efficiency of existing energy sources. Firstly, being enslaved to the relatively short absorption wavelength of most solar energy conversion materials, the utilization of solar energy in the NIR region is limited by far. To vitalize the sunlight in the NIR region, long-wavelength absorbed AIEgens possessing high extinction coefficient and broad absorption spectra covering NIR-I (700–900 nm) or even NIR-II (1000–1700 nm) regions are desired. To this end, the rational integration of strong D–A interaction and large π-conjugation into the molecular skeleton of AIEgens has been proven to be a significant strategy.[210] Besides, preparing AIE-active conjugated polymers represents an alternative approach to enhancing the molar extinction coefficient[211,212] as well as the light-harvesting capacity. Secondly, the flexible design strategies in exploiting high-efficiency and reversible mechanical luminescent AIEgens with desirable sensitivity should be strengthened. For instance, the AIEgens could be constructed on soft and elastic frames, such as MOFs, COFs, and HOFs, to simultaneously maintain the sensitive response and reversible deformation.[148,213] The improved responsiveness is expected to lay a solid foundation for the further exploitation of AIEgens-based wearable devices, which have captivated increasing attention in the field of modern healthcare. Thirdly, for the EL device, the disordered structures of AIEgens in the solid state would restrict the electron–hole mobility, reducing the exciton utilization efficiency. In this regard, large conjugated polycyclic

4870 | *J. Mater. Chem. A*, 2023, **11**, 4850–4875

This journal is © The Royal Society of Chemistry 2023

aromatic hydrocarbons could be introduced on the molecular skeleton[165] to tune the charge carriers of AIEgens in the emissive layer in pursuit of high efficiency. Finally, the organic HTMs of solar cells showed less stability compared to the inorganic HTMs in practical applications. Some strategies such as doping V_2O_5 [214] nanoparticles or small molecules such as $Zn(TFSI)_2$,[215] MoO_3 [216] and 4-*tert*-butylpyridine[217] into HTMs, adding UV filters[218,219] as protectors or employing AIE polymers[220] as HTMs could be considered to improve the formability, aging resistance, and long-term morphological stability of AIEgens-based HTMs. We hope that this review will provide a brand-new perspective for researchers regarding AIEgens and inspire the interdisciplinary scientific community to make a contribution to maintaining global sustainable development.

Author contributions

Xue Li: investigation, visualization, writing–original draft; Hao Yang: data curation, writing–original draft; Ping Zheng: data curation; Danmin Lin: data curation; Zhijun Zhang: conceptualization and data curation; Miaomiao Kang: supervision, funding acquisition, and writing–review & editing; Dong Wang: supervision, funding acquisition, and writing–review & editing; Ben Zhong Tang: visualization and supervision.

Conflicts of interest

There are no conflicts to declare.

Acknowledgements

Notes and references

1 J. Newman, C. A. Bonino and J. A. Trainham, *Annu. Rev. Chem. Biomol. Eng.*, 2018, **9**, 153–174.
2 D. J. Murphy, *Nature*, 2012, **483**, 541.
3 B. Thomas, M. C. Raj, K. B. Athira, M. H. Rubiyah, J. Joy, A. Moores, G. L. Drisko and C. Sanchez, *Chem. Rev.*, 2018, **118**, 11575–11625.
4 W. J. Liu, H. Jiang and H. Q. Yu, *Green Chem.*, 2015, **17**, 4888–4907.
5 M. Q. Zhao, Q. Zhang, J. Q. Huang and F. Wei, *Adv. Funct. Mater.*, 2012, **22**, 675–694.
6 N. L. Panwar, S. C. Kaushik and S. Kothari, *Renewable Sustainable Energy Rev.*, 2011, **15**, 1513–1524.
7 S. Chu, Y. Cui and N. Liu, *Nat. Mater.*, 2017, **16**, 16–22.
8 L. Protesescu, S. Yakunin, M. I. Bodnarchuk, F. Krieg, R. Caputo, C. H. Hendon, R. X. Yang, A. Walsh and M. V. Kovalenko, *Nano Lett.*, 2015, **15**, 3692–3696.
9 F. Y. Cheng, J. Liang, Z. L. Tao and J. Chen, *Adv. Mater.*, 2011, **23**, 1695–1715.
10 R. M. Elavarasan, V. Mudgal, L. Selvamanohar, K. Wang, G. Huang, G. M. N. Shafiullah, C. Markides, K. S. Reddy and M. Nadarajah, *Energy Convers. Manage.*, 2022, **255**, 115278.
11 R. Naveenkumar, M. Ravichandran, V. Mohanavel, A. Karthick, L. Aswin, S. S. H. Priyanka, S. K. Kumar and S. P. Kumar, *Environ. Sci. Pollut. Res. Int.*, 2022, **29**, 9491–9532.
12 M. A. Baldo, D. F. O'Brien, Y. You, A. Shoustikov, S. Sibley, M. E. Thompson and S. R. Forrest, *Nature*, 1998, **395**, 151–154.
13 J. Zhou, Q. Liu, W. Feng, Y. Sun and F. Y. Li, *Chem. Rev.*, 2015, **115**, 395–465.
14 W. Zhao, Z. Liu, J. Yu, X. Lu, J. W. Y. Lam, J. Sun, Z. He, H. Ma and B. Z. Tang, *Adv. Mater.*, 2021, **33**, e2006844.
15 L. Yang, X. J. Wang, G. Z. Zhang, X. F. Chen, G. Q. Zhang and J. Jiang, *Nanoscale*, 2016, **8**, 17422–17426.
16 H. Q. Peng, L. Y. Niu, Y. Z. Chen, L. Z. Wu, C. H. Tung and Q. Z. Yang, *Chem. Rev.*, 2015, **115**, 7502–7542.
17 L. Dong, H. Q. Peng, L. Y. Niu and Q. Z. Yang, *Top. Curr. Chem.*, 2021, **379**, 18.
18 J. Mei, N. L. Leung, R. T. Kwok, J. W. Lam and B. Z. Tang, *Chem. Rev.*, 2015, **115**, 11718–11940.
19 J. Mei, Y. N. Hong, J. W. Y. Lam, A. J. Qin, Y. H. Tang and B. Z. Tang, *Adv. Mater.*, 2014, **26**, 5429–5479.
20 Z. Zhao, H. Zhang, J. W. Y. Lam and B. Z. Tang, *Angew. Chem., Int. Ed.*, 2020, **59**, 9888–9907.
21 T. Han, D. Y. Yan, Q. Wu, N. Song, H. K. Zhang and D. Wang, *Chin. J. Chem.*, 2021, **39**, 677–689.
22 M. M. Kang, Z. J. Zhang, N. Song, M. Li, P. P. Sun, X. H. Chen, D. Wang and B. Z. Tang, *Aggregate*, 2020, **1**, 80–106.
23 Z. Zhang, M. Kang, H. Tan, N. Song, M. Li, P. Xiao, D. Yan, L. Zhang, D. Wang and B. Z. Tang, *Chem. Soc. Rev.*, 2022, **51**, 1983–2030.
24 R. Hu, N. L. C. Leung and B. Z. Tang, *Chem. Soc. Rev.*, 2014, **43**, 4494–4562.
25 M. M. Kang, Z. J. Zhang, W. H. Xu, H. F. Wen, W. Zhu, Q. Wu, H. Z. Wu, J. Y. Gong, Z. J. Wang, D. Wang and B. Z. Tang, *Adv. Sci.*, 2021, **8**, 2100524.
26 N. Song, Z. Zhang, P. Liu, Y. W. Yang, L. Wang, D. Wang and B. Z. Tang, *Adv. Mater.*, 2020, **32**, e2004208.
27 Y. Yuan, C. J. Zhang, M. Gao, R. Zhang, B. Z. Tang and B. Liu, *Angew. Chem., Int. Ed.*, 2015, **54**, 1780–1786.
28 H. T. Feng, Y. X. Yuan, J. B. Xiong, Y. S. Zheng and B. Z. Tang, *Chem. Soc. Rev.*, 2018, **47**, 7452–7476.
29 Y. Zhao, L. P. Zhang, Y. L. Liu, Z. W. Deng, R. Y. Zhang, S. W. Zhang, W. He, Z. J. Qiu, Z. Zhao and B. Z. Tang, *Langmuir*, 2022, **38**, 8719–8732.
30 J. Gong, C. Li and M. R. Wasielewski, *Chem. Soc. Rev.*, 2019, **48**, 1862–1864.

This journal is © The Royal Society of Chemistry 2023

J. Mater. Chem. A, 2023, **11**, 4850–4875 | **4871**

31 A. Shahsavari and M. Akbari, *Renewable Sustainable Energy Rev.*, 2018, **90**, 275–291.

32 Q. Wang, C. Pornrungroj, S. Linley and E. Reisner, *Nat. Energy*, 2022, **7**, 13–24.

33 M. Kang, C. Zhou, S. Wu, B. Yu, Z. Zhang, N. Song, M. M. S. Lee, W. Xu, F. J. Xu, D. Wang, L. Wang and B. Z. Tang, *J. Am. Chem. Soc.*, 2019, **141**, 16781–16789.

34 Y. Wang, Y. Yang, Y. Shi, H. Song and C. Yu, *Adv. Mater.*, 2020, **32**, e1904106.

35 Z. Zhang, W. Xu, P. Xiao, M. Kang, D. Yan, H. Wen, N. Song, D. Wang and B. Z. Tang, *ACS Nano*, 2021, **15**, 10689–10699.

36 C. Yang, C. Ren, J. Zhou, J. Liu, Y. Zhang, F. Huang, D. Ding, B. Xu and J. Liu, *Angew. Chem., Int. Ed.*, 2017, **56**, 2356–2360.

37 R. Dong, Y. Li, M. Chen, P. Xiao, Y. Wu, K. Zhou, Z. Zhao and B. Z. Tang, *Small Methods*, 2022, **6**, e2101247.

38 T. Zhou, R. Hu, L. Wang, Y. Qiu, G. Zhang, Q. Deng, H. Zhang, P. Yin, B. Situ, C. Zhan, A. Qin and B. Z. Tang, *Angew. Chem., Int. Ed.*, 2020, **59**, 9952–9956.

39 L. Liao, W. Xiao, M. Zhao, X. Yu, H. Wang, Q. Wang, S. Chu and Y. Cui, *ACS Nano*, 2020, **14**, 6348–6356.

40 P. Tang, Z. Zhang, A. Y. El-Moghazy, N. Wisuthiphaet, N. Nitin and G. Sun, *ACS Appl. Mater. Interfaces*, 2020, **12**, 49442–49451.

41 C. D. Zangmeister, J. G. Radney, E. P. Vicenzi and J. L. Weaver, *ACS Nano*, 2020, **14**, 9188–9200.

42 S. Feng, C. Shen, N. Xia, W. Song, M. Fan and B. J. Cowling, *Lancet Respir. Med.*, 2020, **8**, 434–436.

43 L. Huang, S. Xu, Z. Wang, K. Xue, J. Su, Y. Song, S. Chen, C. Zhu, B. Z. Tang and R. Ye, *ACS Nano*, 2020, **14**, 12045–12053.

44 J. Sun, Y. Bai, E. Y. Yu, G. Ding, H. Zhang, M. Duan, P. Huang, M. Zhang, H. Jin, R. T. Kwok, Y. Li, G. G. Shan, B. Z. Tang and H. Wang, *Biomaterials*, 2022, **291**, 121898.

45 B. Li, D. Wang, M. M. S. Lee, W. Wang, Q. Tan, Z. Zhao, B. Z. Tang and X. Huang, *ACS Nano*, 2021, **15**, 13857–13870.

46 M. Li, H. Wen, H. Li, Z. C. Yan, Y. Li, L. Wang, D. Wang and B. Z. Tang, *Biomaterials*, 2021, **276**, 121007.

47 T. Oki and S. Kanae, *Science*, 2006, **313**, 1068–1072.

48 M. Rodell, J. S. Famiglietti, D. N. Wiese, J. T. Reager, H. K. Beaudoing, F. W. Landerer and M. H. Lo, *Nature*, 2018, **557**, 651–659.

49 C. J. Vörösmarty, P. Green, J. Salisbury and R. B. Lammers, *Science*, 2000, **289**, 284–288.

50 Z. Tan, S. Chen, X. Peng, L. Zhang and C. Gao, *Science*, 2018, **360**, 518–521.

51 P. Tao, G. Ni, C. Song, W. Shang, J. Wu, J. Zhu, G. Chen and T. Deng, *Nat. Energy*, 2018, **3**, 1031–1041.

52 A. D. Khawaji, I. K. Kutubkhanah and J.-M. Wie, *Desalination*, 2008, **221**, 47–69.

53 C. Chen, Y. Kuang and L. Hu, *Joule*, 2019, **3**, 683–718.

54 G. Chen, J. Sun, Q. Peng, Q. Sun, G. Wang, Y. Cai, X. Gu, Z. Shuai and B. Z. Tang, *Adv. Mater.*, 2020, **32**, e1908537.

55 H. Li, H. Wen, J. Li, J. Huang, D. Wang and B. Z. Tang, *ACS Appl. Mater. Interfaces*, 2020, **12**, 26033–26040.

56 X. Y. Wang, J. Xue, C. Ma, T. He, H. Qian, B. Wang, J. Liu and Y. Lu, *J. Mater. Chem. A*, 2019, **7**, 16696–16703.

57 H. Li, W. Zhu, M. Li, Y. Li, R. T. K. Kwok, J. W. Y. Lam, L. Wang, D. Wang and B. Z. Tang, *Adv. Mater.*, 2021, **33**, e2102258.

58 J. J. Gallardo-Rodríguez, A. Astuya-Villalón, A. Llanos-Rivera, V. Avello-Fontalba and V. Ulloa-Jofré, *Rev Aquac.*, 2019, **11**, 661–684.

59 J. Huisman, G. A. Codd, H. W. Paerl, B. W. Ibelings, J. M. H. Verspagen and P. M. Visser, *Nat. Rev. Microbiol.*, 2018, **16**, 471–483.

60 W. A. Wurtsbaugh, H. W. Paerl and W. K. Dodds, *Wiley Interdiscip. Rev.: Water*, 2019, **6**, e1373.

61 Q. Yue, X. He, N. Yan, S. Tian, C. Liu, W.-X. Wang, L. Luo and B. Z. Tang, *Chem. Eng. J.*, 2021, **417**, 127890.

62 A. Q. Xie, L. Zhu, Y. Liang, J. Mao, Y. Liu and S. Chen, *Angew. Chem., Int. Ed.*, 2022, **61**, e202208592.

63 H. Li, H. Wen, Z. Zhang, N. Song, R. T. K. Kwok, J. W. Y. Lam, L. Wang, D. Wang and B. Z. Tang, *Angew. Chem., Int. Ed.*, 2020, **59**, 20371–20375.

64 Y. Yang, S. Zhang, X. Zhang, L. Gao, Y. Wei and Y. Ji, *Nat. Commun.*, 2019, **10**, 3165.

65 K. Fu, X. Zeng, X. Zhao, Y. Wu, M. Li, X. S. Li, C. Pan, Z. Chen and Z. Q. Yu, *Small*, 2021, **17**, e2103172.

66 Y. Liu, H. Yang, Y. Wang, C. Ma, S. Luo, Z. Wu, Z. Zhang, W. Li and S. Liu, *Chem. Eng. J.*, 2021, **424**, 130426.

67 T. E. Miller, T. Beneyton, T. Schwander, C. Diehl, M. Girault, R. McLean, T. Chotel, P. Claus, N. S. Cortina, J. C. Baret and T. J. Erb, *Science*, 2020, **368**, 649–654.

68 H. Kirchhoff, *New Phytol.*, 2019, **223**, 565–574.

69 X. Zhou, Y. Zeng, F. Lv, H. Bai and S. Wang, *Acc. Chem. Res.*, 2022, **55**, 156–170.

70 F. Abiusi, R. H. Wijffels and M. Janssen, *ACS Sustainable Chem. Eng.*, 2020, **8**, 6065–6074.

71 T. G. Hwang, G.-Y. Kim, J.-I. Han, S. Kim and J. P. Kim, *ACS Sustainable Chem. Eng.*, 2020, **8**, 15888–15897.

72 E. H. White and D. F. Roswell, *J. Am. Chem. Soc.*, 1967, **89**, 3944–3945.

73 X. Zhen, C. Zhang, C. Xie, Q. Miao, K. L. Lim and K. Pu, *ACS Nano*, 2016, **10**, 6400–6409.

74 S. Ye, N. Hananya, O. Green, H. Chen, A. Q. Zhao, J. Shen, D. Shabat and D. Yang, *Angew. Chem., Int. Ed.*, 2020, **59**, 14326–14330.

75 Q. Chi, W. Chen and Z. He, *Luminescence*, 2015, **30**, 990–995.

76 Q. Li, F. Li, W. Shen, X. Liu and H. Cui, *J. Mater. Chem. C*, 2016, **4**, 3477–3484.

77 C. Wang, Y. Lan, F. Yuan, T. H. Fereja, B. Lou, S. Han, J. Li and G. Xu, *Microchim. Acta*, 2019, **187**, 1–6.

78 Z. F. Zhang, H. Cui, C. Z. Lai and L. J. Liu, *Anal. Chem.*, 2005, **77**, 3324–3329.

79 L. Deng, Y. Wu, S. Xu, Y. Tang, X. Zhang and P. Wu, *ACS Sens.*, 2018, **3**, 1190–1195.

80 X. Li, H. Zhang, Y. Tang, P. Wu, S. Xu and X. Zhang, *ACS Sens.*, 2017, **2**, 810–816.

81 D. Yang, Y. He and F. Chen, *Luminescence*, 2017, **32**, 1077–1083.

4872 | *J. Mater. Chem. A*, 2023, **11**, 4850–4875

This journal is © The Royal Society of Chemistry 2023

82 M. E. Quimbar, S. Q. Davis, S. T. Al-Farra, A. Hayes, V. Jovic, M. Masuda and A. R. Lippert, *Anal. Chem.*, 2020, **92**, 14594–14600.

83 S. N. A. Shah, Y. Zheng, H. Li and J. M. Lin, *J. Phys. Chem. C*, 2016, **120**, 9308–9316.

84 J. Shu, Z. Qiu, Q. Zhou, Y. Lin, M. Lu and D. Tang, *Anal. Chem.*, 2016, **88**, 2958–2966.

85 S. X. Liang, H. Li and J. M. Lin, *Luminescence*, 2008, **23**, 381–385.

86 R. Singh, B. B. Krishna, J. Kumar and T. Bhaskar, *Bioresour. Technol.*, 2016, **199**, 398–407.

87 R. Freeman, X. Liu and I. Willner, *J. Am. Chem. Soc.*, 2011, **133**, 11597–11604.

88 J. S. Lee, H. A. Joung, M. G. Kim and C. B. Park, *ACS Nano*, 2012, **6**, 2978–2983.

89 M. Yang, J. Huang, J. Fan, J. Du, K. Pu and X. Peng, *Chem. Soc. Rev.*, 2020, **49**, 6800–6815.

90 C. Chen, H. Gao, H. Ou, R. T. K. Kwok, Y. Tang, D. Zheng and D. Ding, *J. Am. Chem. Soc.*, 2022, **144**, 3429–3441.

91 J. Lou, X. Tang, H. Zhang, W. Guan and C. Lu, *Angew. Chem., Int. Ed.*, 2021, **60**, 13029–13034.

92 A. Abbott, *Nature*, 2009, **461**, 706–707.

93 Z. Liu, F. Zhao, S. Gao, J. Shao and H. Chang, *Nanoscale Res. Lett.*, 2016, **11**, 1–8.

94 M. Zhu, J. Lu, Y. Hu, Y. Liu, S. Hu and C. Zhu, *Environ. Sci. Pollut. Res. Int.*, 2020, **27**, 31289–31299.

95 J. Niu, J. Fan, X. Wang, Y. Xiao, X. Xie, X. Jiao, C. Sun and B. Tang, *Anal. Chem.*, 2017, **89**, 7210–7215.

96 M. J. Daniels, Y. Wang, M. Lee and A. R. Venkitaraman, *Science*, 2004, **306**, 876–879.

97 E. P. Randviir and C. E. Banks, *Sens. Actuators, B*, 2013, **183**, 239–252.

98 R. Jalili and A. Khataee, *Microchim. Acta*, 2019, **186**, 1–9.

99 Z. Li, W. Qin, J. Wu, Z. Yang, Z. Chi and G. Liang, *Mater. Chem. Front.*, 2019, **3**, 2051–2057.

100 T. Zhou, Q. Wang, M. Liu, Z. Liu, Z. Zhu, X. Zhao and W. H. Zhu, *Aggregate*, 2021, **2**, e22.

101 A. P. Côté, A. I. Benin, N. W. Ockwig, M. O'Keeffe, A. J. Matzger and O. M. Yaghi, *Science*, 2005, **310**, 1166–1170.

102 H. Tan and Y. Li, *Microchim. Acta*, 2021, **188**, 1–10.

103 V. Michopoulos, A. Powers, C. F. Gillespie, K. J. Ressler and T. Jovanovic, *Neuropsychopharmacology*, 2017, **42**, 254–270.

104 M. Leslie, *Science*, 2015, **347**, 18–21.

105 D. A. Hammoud, *J. Nucl. Med.*, 2016, **57**, 1161–1165.

106 S. Zhang, H. Cui, M. Gu, N. Zhao, M. Cheng and J. Lv, *Small*, 2019, **15**, e1804662.

107 Y. H. Seo, A. Singh, H. J. Cho, Y. Kim, J. Heo, C. K. Lim, S. Y. Park, W. D. Jang and S. Kim, *Biomaterials*, 2016, **84**, 111–118.

108 H. Shen, F. Sun, X. Zhu, J. Zhang, X. Ou, J. Zhang, C. Xu, H. H. Y. Sung, I. D. Williams, S. Chen, R. T. K. Kwok, J. W. Y. Lam, J. Sun, F. Zhang and B. Z. Tang, *J. Am. Chem. Soc.*, 2022, **144**, 15391–15402.

109 L. A. Torre, R. L. Siegel, E. M. Ward and A. Jemal, *Cancer Epidemiol., Biomarkers Prev.*, 2016, **25**, 16–27.

110 E. A. Sarma, S. C. Kobrin and M. J. Thompson, *Cancer Prev. Res.*, 2020, **13**, 715–720.

111 G. Rompianesi, F. Pegoraro, C. D. Ceresa, R. Montalti and R. I. Troisi, *World J. Gastroenterol.*, 2022, **28**, 108–122.

112 C. Liu, X. Wang, J. Liu, Q. Yue, S. Chen, J. W. Y. Lam, L. Luo and B. Z. Tang, *Adv. Mater.*, 2020, **32**, e2004685.

113 Y. Zhang, C. Yan, C. Wang, Z. Guo, X. Liu and W. H. Zhu, *Angew. Chem., Int. Ed.*, 2020, **59**, 9059–9066.

114 X. Ni, X. Zhang, X. Duan, H. L. Zheng, X. S. Xue and D. Ding, *Nano Lett.*, 2019, **19**, 318–330.

115 D. Mao, W. Wu, S. Ji, C. Chen, F. Hu, D. Kong, D. Ding and B. Liu, *Chem*, 2017, **3**, 991–1007.

116 L. Farzin, M. Shamsipur, S. Sheibani, L. Samandari and Z. Hatami, *Microchim. Acta*, 2019, **186**, 1–27.

117 Q. Wu, G. Li, S. Wang, K. Liu and J. Hao, *Environ. Sci. Technol.*, 2018, **52**, 12368–12375.

118 Z. Wang, J. Pan, Q. Li, Y. Zhou, S. Yang, J.-J. Xu and D. Hua, *Adv. Funct. Mater.*, 2020, **30**, 2000220.

119 Y. Chen, A. J. Spiering, S. Karthikeyan, G. W. Peters, E. W. Meijer and R. P. Sijbesma, *Nat. Chem.*, 2012, **4**, 559–562.

120 A. Lavrenova, D. W. Balkenende, Y. Sagara, S. Schrettl, Y. C. Simon and C. Weder, *J. Am. Chem. Soc.*, 2017, **139**, 4302–4305.

121 Y. Sagara, S. Yamane, M. Mitani, C. Weder and T. Kato, *Adv. Mater.*, 2016, **28**, 1073–1095.

122 Y. Xie and Z. Li, *Chem*, 2018, **4**, 943–971.

123 W. Li, Q. Huang, Z. Yang, X. Zhang, D. Ma, J. Zhao, C. Xu, Z. Mao, Y. Zhang and Z. Chi, *Angew. Chem., Int. Ed.*, 2020, **59**, 22645–22651.

124 C. Wang, B. J. Xu, M. S. Li, Z. G. Chi, Y. J. Xie, Q. Q. Li and Z. Li, *Mater. Horiz.*, 2016, **3**, 220–225.

125 W. Li, Q. Huang, Z. Mao, J. Zhao, H. Wu, J. Chen, Z. Yang, Y. Li, Z. Yang, Y. Zhang, M. P. Aldred and Z. Chi, *Angew. Chem., Int. Ed.*, 2020, **59**, 3739–3745.

126 Q. Dang, L. Hu, J. Wang, Q. Zhang, M. Han, S. Luo, Y. Gong, C. Wang, Q. Li and Z. Li, *Chem.–Eur. J.*, 2019, **25**, 7031–7037.

127 Q. Li and Z. Li, *Acc. Chem. Res.*, 2020, **53**, 962–973.

128 Y. Yu, C. Wang, Y. Wei, Y. Y. Fan, J. Yang, J. Q. Wang, M. M. Han, Q. Q. Li and Z. Li, *Adv. Opt. Mater.*, 2019, **7**, 1900505.

129 Z. He, W. Zhao, J. W. Y. Lam, Q. Peng, H. Ma, G. Liang, Z. Shuai and B. Z. Tang, *Nat. Commun.*, 2017, **8**, 1–8.

130 S. Goossens, B. De Pauw, T. Geernaert, M. S. Salmanpour, Z. S. Khodaei, E. Karachalios, D. Saenz-Castillo, H. Thienpont and F. Berghmans, *Smart Mater. Struct.*, 2019, **28**, 065008.

131 H. Mei, M. F. Haider, R. Joseph, A. Migot and V. Giurgiutiu, *Sensors*, 2019, **19**, 383.

132 K. Maity and D. Mandal, *ACS Appl. Mater. Interfaces*, 2018, **10**, 18257–18269.

133 R. J. Greene, A. B. Clarke, S. Turner and E. A. Patterson, *J. Strain Anal. Eng. Des.*, 2007, **42**, 173–182.

134 X. Tang, S. Xu and X. Wang, *Opt. Express*, 2013, **21**, 14303–14315.

135 H. Yuan, K. Wang, K. Yang, B. Liu and B. Zou, *J. Phys. Chem. Lett.*, 2014, **5**, 2968–2973.

This journal is © The Royal Society of Chemistry 2023

J. Mater. Chem. A, 2023, **11**, 4850–4875 | **4873**

136 Z. Qiu, W. Zhao, M. Cao, Y. Wang, J. W. Y. Lam, Z. Zhang, X. Chen and B. Z. Tang, *Adv. Mater.*, 2018, **30**, e1803924.

137 Z. Zhang, M. Cao, L. Zhang, Z. Qiu, W. Zhao, G. Chen, X. Chen and B. Z. Tang, *ACS Appl. Mater. Interfaces*, 2020, **12**, 22129–22136.

138 M. S. Kwon, J. Gierschner, S. J. Yoon and S. Y. Park, *Adv. Mater.*, 2012, **24**, 5487–5492.

139 Q. K. Qi, J. Y. Qian, X. Tan, J. B. Zhang, L. J. Wang, B. Xu, B. Zou and W. J. Tian, *Adv. Funct. Mater.*, 2015, **25**, 4005–4010.

140 L. J. Zhang, Y. Wang, X. Q. Hu and P. F. Xu, *Chem. – Asian J.*, 2016, **11**, 834–838.

141 X. Zhang, Y. Liu, W. Wei, L. Gao, Y. Duan, H. Han and T. Han, *Dyes Pigm.*, 2022, **197**, 109916.

142 W. Zhao, Z. He, Q. Peng, J. W. Y. Lam, H. Ma, Z. Qiu, Y. Chen, Z. Zhao, Z. Shuai, Y. Dong and B. Z. Tang, *Nat. Commun.*, 2018, **9**, 3044.

143 X. Lin, Z. Wu, Y. Wu, M. Xuan and Q. He, *Adv. Mater.*, 2016, **28**, 1060–1072.

144 W. Li, Q. Huang, Z. Mao, Q. Li, L. Jiang, Z. Xie, R. Xu, Z. Yang, J. Zhao, T. Yu, Y. Zhang, M. P. Aldred and Z. Chi, *Angew. Chem., Int. Ed.*, 2018, **57**, 12727–12732.

145 J. Jang, H. Kim, S. Ji, H. J. Kim, M. S. Kang, T. S. Kim, J. e. Won, J. H. Lee, J. Cheon and K. Kang, *Nano Lett.*, 2019, **20**, 66–74.

146 Y. Zhuang and R. J. Xie, *Adv. Mater.*, 2021, **33**, e2005925.

147 C. Wang, Y. Yu, Y. Yuan, C. Ren, Q. Liao, J. Wang, Z. Chai, Q. Li and Z. Li, *Matter*, 2020, **2**, 181–193.

148 Q. Huang, W. Li, Z. Yang, J. Zhao, Y. Li, Z. Mao, Z. Yang, S. Liu, Y. Zhang and Z. Chi, *CCS Chem.*, 2022, **4**, 1643–1653.

149 H. Lee, Z. Jiang, T. Yokota, K. Fukuda, S. Park and T. Someya, *Mater. Sci. Eng., R*, 2021, **146**, 100631.

150 M. X. Yu, R. S. Huang, J. J. Guo, Z. J. Zhao and B. Z. Tang, *Photonix*, 2020, **1**, 1–33.

151 L. Zong, Y. Xie, C. Wang, J.-R. Li, Q. Li and Z. Li, *Chem. Commun.*, 2016, **52**, 11496–11499.

152 Y. Y. Gong, J. Liu, Y. R. Zhang, G. F. He, Y. Lu, W. B. Fan, W. Z. Yuan, J. Z. Sun and Y. M. Zhang, *J. Mater. Chem. C*, 2014, **2**, 7552–7560.

153 J. Mei, Y. Huang and H. Tian, *ACS Appl. Mater. Interfaces*, 2018, **10**, 12217–12261.

154 H. L. Mao, Y. P. Li, Y. H. Zhang, L. W. Kong, Y. Tian, J. B. Shi, Z. X. Cai, B. Tong and Y. P. Dong, *Dyes Pigm.*, 2020, **175**, 108169.

155 G. Hong, X. Gan, C. Leonhardt, Z. Zhang, J. Seibert, J. M. Busch and S. Bräse, *Adv. Mater.*, 2021, **33**, 2005630.

156 S. Wang, H. Zhang, B. Zhang, Z. Xie and W.-Y. Wong, *Mater. Sci. Eng., R*, 2020, **140**, 100547.

157 S. Kappaun, C. Slugovc and E. J. W. List, *Int. J. Mol. Sci.*, 2008, **9**, 1527–1547.

158 H. R. Wang, H. Xing, J. Y. Gong, H. K. Zhang, J. Zhang, P. F. Wei, G. J. Yang, J. W. Y. Lam, R. Lu and B. Z. Tang, *Mater. Horiz.*, 2020, **7**, 1566–1572.

159 W. Z. Yuan, X. Bin, G. Chen, Z. H. He, J. Liu, H. L. Ma, Q. Peng, B. W. Wei, Y. Y. Gong, Y. W. Lu, G. F. He and Y. M. Zhang, *Adv. Opt. Mater.*, 2017, **5**, 1700466.

160 J. Yang, Z. G. Chi, W. H. Zhu, B. Z. Tang and Z. Li, *Sci. China: Chem.*, 2019, **62**, 1090–1098.

161 J. J. Zeng, J. J. Guo, H. Liu, Z. J. Zhao and B. Tang, *Adv. Funct. Mater.*, 2020, **30**, 2000019.

162 Z. H. Wu, Z. T. Huang, R. X. Guo, C. L. Sun, L. C. Chen, B. Sun, Z. F. Shi, X. F. Shao, H. Y. Li and H. L. Zhang, *Angew. Chem., Int. Ed.*, 2017, **56**, 13031–13035.

163 G. Cai, P. Xue, Z. Chen, T. Li, K. Liu, W. Ma, J. Lian, P. Zeng, Y. Wang and R. P. Han, *Chem. Mater.*, 2018, **31**, 6484–6490.

164 M. M. Islam, Z. Hu, Q. S. Wang, C. Redshaw and X. Feng, *Mater. Chem. Front.*, 2019, **3**, 762–781.

165 J. Zeng, N. L. Qiu, J. Y. Zhang, X. H. Wang, C. Redshaw, X. Feng, J. W. Y. Lam, Z. J. Zhao and B. Z. Tang, *Adv. Opt. Mater.*, 2022, **10**, 2200917.

166 Z. Wang, C. Y. Zhu, J. T. Mo, P. Y. Fu, Y. W. Zhao, S. Y. Yin, J. J. Jiang, M. Pan and C. Y. Su, *Angew. Chem., Int. Ed.*, 2019, **58**, 9752–9757.

167 X. Hu, Z. Wang, B. Lin, C. Zhang, L. Cao, T. Wang, J. Zhang, C. Wang and W. Lin, *Chem. - Eur. J.*, 2017, **23**, 8390–8394.

168 S.-S. Zhao, H. Zhang, L. Wang, L. Chen and Z. Xie, *J. Mater. Chem. C*, 2018, **6**, 11701–11706.

169 Q. Gong, Z. Hu, B. J. Deibert, T. J. Emge, S. J. Teat, D. Banerjee, B. Mussman, N. D. Rudd and J. Li, *J. Am. Chem. Soc.*, 2014, **136**, 16724–16727.

170 H. Ding, J. Li, G. Xie, G. Lin, R. Chen, Z. Peng, C. Yang, B. Wang, J. Sun and C. Wang, *Nat. Commun.*, 2018, **9**, 5234.

171 Y. Xu, F. Zhang and X. Feng, *Small*, 2011, **7**, 1338–1360.

172 Y. W. Liu, Y. L. Guo and Y. Q. Liu, *Small Struct.*, 2021, **2**, 2000083.

173 Z. T. Liu, G. X. Zhang and D. Q. Zhang, *Chem. – Eur. J.*, 2016, **22**, 462–471.

174 C. Zhang, P. Chen and W. Hu, *Small*, 2016, **12**, 1392.

175 Y. Y. Li, S. J. Liu, H. W. Ni, H. Zhang, H. Q. Zhang, C. Chuah, C. Ma, K. S. Wong, J. W. Y. Lam, R. T. K. Kwok, J. Qian, X. F. Lu and B. Z. Tang, *Angew. Chem., Int. Ed.*, 2020, **59**, 12822–12826.

176 Z. Zhao, S. M. Gao, X. Y. Zheng, P. F. Zhang, W. T. Wu, R. T. K. Kwok, Y. Xiong, N. L. C. Leung, Y. C. Chen, X. K. Gao, J. W. Y. Lam and B. Z. Tang, *Adv. Funct. Mater.*, 2018, **28**, 1705609.

177 K. Ichimura, *Chem. Rev.*, 2000, **100**, 1847–1874.

178 H. Coles and S. Morris, *Nat. Photonics*, 2010, **4**, 676–685.

179 C. Keum, D. Becker, E. Archer, H. Bock, H. Kitzerow, M. C. Gather and C. Murawski, *Adv. Opt. Mater.*, 2020, **8**, 2000414.

180 Y. L. Li, N. N. Li, D. Wang, F. Chu, S. D. Lee, Y. W. Zheng and Q.-H. Wang, *Light: Sci. Appl.*, 2022, **11**, 188.

181 H. W. Chen, J. H. Lee, B. Y. Lin, S. Chen and S. T. Wu, *Light: Sci. Appl.*, 2018, **7**, 17168.

182 Y. Chen, P. Lu, Z. Li, Y. Yuan, Q. Ye and H. Zhang, *ACS Appl. Mater. Interfaces*, 2020, **12**, 56604–56614.

183 P. Goel and M. Arora, *RSC Adv.*, 2015, **5**, 14974–14981.

184 S. Yamane, Y. Sagara, T. Mutai, K. Araki and T. Kato, *J. Mater. Chem. C*, 2013, **1**, 2648–2656.

185 M. Zhu, Y. Chen, X. Zhang, M. Chen, H. Guo and F. Yang, *Soft Matter*, 2018, **14**, 6737–6744.

4874 | *J. Mater. Chem. A*, 2023, **11**, 4850–4875

This journal is © The Royal Society of Chemistry 2023

186 Y. Wang, Y. Liao, C. P. Cabry, D. Zhou, G. Xie, Z. Qu, D. W. Bruce and W. Zhu, *J. Mater. Chem. C*, 2017, **5**, 3999–4008.

187 H. Guo, S. Zheng, S. Chen, C. Han and F. Yang, *Soft Matter*, 2019, **15**, 8329–8337.

188 D. Zhao, F. Fan, J. Cheng, Y. Zhang, K. S. Wong, V. G. Chigrinov, H. S. Kwok, L. Guo and B. Z. Tang, *Adv. Opt. Mater.*, 2015, **3**, 199–202.

189 X. Zhang, W. Qin, B. Cheng, H. Guo and F. Yang, *J. Mol. Liq.*, 2020, **298**, 112074.

190 K. Liu, Y. Shen, X. Li, Y. Zhang, Y. Quan and Y. Cheng, *Chem. Commun.*, 2020, **56**, 12829–12832.

191 F. Song, Y. Cheng, Q. Liu, Z. Qiu, J. W. Lam, L. Lin, F. Yang and B. Z. Tang, *Mater. Chem. Front.*, 2019, **3**, 1768–1778.

192 Q. Xia, L. Meng, T. He, G. Huang, B. S. Li and B. Z. Tang, *ACS Nano*, 2021, **15**, 4956–4966.

193 H. Ruan, G. Chen, X. Zhao, Y. Wang, Y. Liao, H. Peng, C. L. Feng, X. Xie and II. Smalyukh, *ACS Appl. Mater. Interfaces*, 2018, **10**, 43184–43191.

194 X. Meng, L. Zhang, Y. Xie, X. Hu, Z. Xing, Z. Huang, C. Liu, L. Tan, W. Zhou, Y. Sun, W. Ma and Y. Chen, *Adv. Mater.*, 2019, **31**, e1903649.

195 A. K. Jena, A. Kulkarni and T. Miyasaka, *Chem. Rev.*, 2019, **119**, 3036–3103.

196 S. E. Hosseini and M. A. Wahid, *Int. J. Energy Res.*, 2020, **44**, 4110–4131.

197 R. Sharma, A. Sharma, S. Agarwal and M. S. Dhaka, *Sol. Energy*, 2022, **244**, 516–535.

198 C. C. Chen, W. H. Chang, K. Yoshimura, K. Ohya, J. You, J. Gao, Z. Hong and Y. Yang, *Adv. Mater.*, 2014, **26**, 5670–5677.

199 W. Gao, F. Qi, Z. Peng, F. R. Lin, K. Jiang, C. Zhong, W. Kaminsky, Z. Guan, C. S. Lee, T. J. Marks, H. Ade and A. K. Jen, *Adv. Mater.*, 2022, **34**, e2202089.

200 Z. Duan, X. Liang, Y. Feng, H. Ma, B. Liang, Y. Wang, S. Luo, S. Wang, R. E. Schropp and Y. Mai, *Adv. Mater.*, 2022, **34**, 2202969.

201 L. Calió, S. Kazim, M. Grätzel and S. Ahmad, *Angew. Chem., Int. Ed.*, 2016, **55**, 14522–14545.

202 P. K. Kung, M. H. Li, P. Y. Lin, Y. H. Chiang, C. R. Chan, T. F. Guo and P. Chen, *Adv. Mater. Interfaces*, 2018, **5**, 1800882.

203 T. H. Schloemer, J. A. Christians, J. M. Luther and A. Sellinger, *Chem. Sci.*, 2019, **10**, 1904–1935.

204 J. Cornil, D. Beljonne, J. P. Calbert and J. L. Brédas, *Adv. Mater.*, 2001, **13**, 1053–1067.

205 G. Han, Y. Guo, X. Song, Y. Wang and Y. Yi, *J. Mater. Chem. C*, 2017, **5**, 4852–4857.

206 Y. Cao, W. Chen, H. Sun, D. Wang, P. Chen, A. B. Djurišić, Y. Zhu, B. Tu, X. Guo and B.-Z. Tang, *Sol. RRL*, 2020, **4**, 1900189.

207 O. R. Yamilova, I. V. Martynov, A. S. Brandvold, I. V. Klimovich, A. H. Balzer, A. V. Akkuratov, I. E. Kusnetsov, N. Stingelin and P. A. Troshin, *Adv. Mater. Interfaces*, 2020, **10**, 1903163.

208 Q. Burlingame, M. Ball and Y. L. Loo, *Nat. Energy*, 2020, **5**, 947–949.

209 L. Zeng, L. F. Zhang, L. C. Mao, X. T. Hu, Y. Wei, L. C. Tan and Y. W. Chen, *Adv. Opt. Mater.*, 2022, **10**, 2200968.

210 Kenry, B. Z. Tang and B. Liu, *Chem*, 2020, **6**, 1195–1198.

211 G. Feng, G. Q. Zhang and D. Ding, *Chem. Soc. Rev.*, 2020, **49**, 8179–8234.

212 W. Wu, G. C. Bazan and B. Liu, *Chem*, 2017, **2**, 760–790.

213 Y.-R. Jia, G. L. Gao, K. Xu and M. Xia, *Dyes Pigm.*, 2022, **205**, 110479.

214 S. Rafique, S. M. Abdullah, W. E. Mahmoud, A. A. Al-ghamdi and K. J. R. A. Sulaiman, *RSC Adv.*, 2016, **6**, 50043–50052.

215 J. Y. Seo, H. S. Kim, S. Akin, M. Stojanovic, E. Simon, M. Fleischer, A. Hagfeldt, S. Zakeeruddin and M. Grätzel, *Energy Environ. Sci.*, 2018, **11**, 2985–2992.

216 J. Xu, O. Voznyy, R. Comin, X. Gong, G. Walters, M. Liu, P. Kanjanaboos, X. Lan and E. H. Sargent, *Adv. Mater.*, 2016, **28**, 2807–2815.

217 S. Wang, M. Sina, P. Parikh, T. Uekert, B. Shahbazian, A. Devaraj and Y. S. Meng, *Nano Lett.*, 2016, **16**, 5594–5600.

218 H. Kimura, K. Fukuda, H. Jinno, S. Park, M. Saito, I. Osaka, K. Takimiya, S. Umezu and T. Someya, *Adv. Mater.*, 2019, **31**, e1808033.

219 G. Aljaiuossi, Y. F. Makableh and M. Al-Fandi, *Semicond. Sci. Technol.*, 2019, **34**, 125014.

220 Y. Yao, C. Cheng, C. Zhang, H. Hu, K. Wang and S. De Wolf, *Adv. Mater.*, 2022, **34**, e2203794.

This journal is © The Royal Society of Chemistry 2023

J. Mater. Chem. A, 2023, **11**, 4850–4875 | **4875**